Master's thesis

2019

Emma Eng Berge

NTNU
Norwegian University of
Science and Technology
Faculty of Natural Sciences
Department of Materials Science and Engineering

Emma Eng Berge

Synthesis and thermal decomposition of sodium rare-earth borohydride halides

June 2019

NTNU
Norwegian University of
Science and Technology

NTNU
Norwegian University of
Science and Technology

NTNU

Norwegian University of
Science and Technology

Synthesis and thermal decomposition of sodium rare-earth borohydride halides

Emma Eng Berge

Chemical Engineering and Biotechnology
Submission date: June 2019
Supervisor: Tor Grande, IMA
Co-supervisor: Magnus H. Sørby, Institute for Energy Technology
Magnus M. Nygård, Institute for Energy Technology

Norwegian University of Science and Technology
Department of Materials Science and Engineering

Preface

This master thesis presents the work conducted during the last semester of a 5-year Master's program in Chemical Engineering and Biotechnology at the Norwegian University of Science and Technology. The project is a collaboration between the Department of Materials Science and Engineering at NTNU and the Department of Neutron Materials Characterization at the Institute for Energy Technology. The present work is a continuation of the Fall 2018 Specialization project, *Synthesis and characterization of sodium rare-earth borohydride halides*. That project concerned synthesis and room temperature characterization of several samples in the system, $NaBH_4$-REI_3 (RE = Y, Ce, Pr, Nd, Gd, Tb and Er). This Master project reports on the decomposition behavior of those materials. In addition, the study is extended to include samples from the systems $NaBH_4$-$RECl_3$ with RE = Ce, Tb and Yb.

I owe a great debt of gratitude to my supervisors Tor Grande at NTNU and Magnus H. Sørby at IFE, for the expertise and assistance you have provided during the process of writing this thesis. Furthermore, I would like to thank Magnus M. Nygård, who has assisted me numerous times and been a valuable discussion partner. Lastly, I would like to express my appreciation to Bjørn Hauback for giving me the opportunity to write my thesis in such an insightful and supportive environment as IFE.

Kjeller, 2019

Emma Eng Berge

Abstract

Rare-earth borohydrides have attracted great interest for energy storage applications due to large hydrogen content and good Li-ion conductivity. However, so far the temperatures for hydrogen release are too high, and the re-hydrogenation properties are too poor for practical hydrogen storage purposes. In this thesis, the thermal stability and decomposition route of $Na_2RE_2(BH_4)_5I_3$ where *RE* = Ce, Pr, Nd, Gd, and Tb, were investigated by in-situ synchrotron radiation powder X-ray diffraction (SR-PXD), thermogravimetric analysis (TGA) and differential scanning calorimetry (DSC). The results showed that the onset temperature for the decomposition of $Na_2RE_2(BH_4)_5I_3$ did not systematically change with increased Pauling electronegativity of the rare-earth cation. It was also observed that the activation energies for the decomposition had a positive and almost linear correlation with the cation electronegativity. Bragg reflections from unknown phases appeared in several of the samples during heating.

High energy ball-milling of $NaBH_4$ and $RECl_3$ (*RE* = Tb and Yb) in the molar ratio 3:1 was also conducted. An additional synthesis of $NaBH_4$ and $CeCl_3$ in the molar ratio 5:3 was attempted as well. The phase composition and their crystal structures were determined by room temperature SR-PXD. The synthesis resulted in the formation of two previously unreported phases $NaTb(BH_4)_2Cl_2$ and $NaYb(BH_4)_2Cl_2$. Both were isostructural with the previously reported monoclinic phase $NaY(BH_4)_2Cl_2$ (space group $P2/c$). The samples with $TbCl_3$ and $YbCl_3$ also contained the Na_3RECl_6 phase and significant amounts of the starting materials. Large amounts of $CeCl_3$ and a solid-solution of $NaBH_4$ and NaCl were observed for the sample with $CeCl_3$.

The thermal stability and decomposition routes of the chloride containing samples were investigated in the same manner as the $Na_2RE_2(BH_4)_5I_3$ phases. The measurements indicated that the decomposition routes for $NaTb(BH_4)_2Cl_2$ and $NaYb(BH_4)_2Cl_2$ were considerably different. $NaTb(BH_4)_2Cl_2$ decomposed in a single step while the decomposition route of $NaYb(BH_4)_2Cl_2$ consisted of multiple steps.

Sammendrag

Sjeldne jordarts borhydrider har tiltrukket seg stor interesse på grunn av deres mulighet for energilagring. Materialene har et høyt hydrogeninnhold og gode ledningsevner for Li-ioner. Det kreves imidlertid høye temperaturer for hydrogenutslipp, i tillegg til at re-hydrogeneringsegenskapene er for dårlige til praktiske hydrogenlagringsformål. I denne oppgaven ble den termiske stabiliteten og dekomponeringsforløpet av $Na_2RE_2(BH_4)_5I_3$ hvor *RE* = Ce, Pr, Nd, Gd and Tb, analysert ved hjelp av in-situ pulverdiffraksjon fra synkrotronstråling (SR-PXD), termogravimetrisk analyse (TGA) og differensial sveipe kalorimetri (DSC). Resultatene viste at starttemperaturen for dekomponeringen av $Na_2RE_2(BH_4)_5I_3$ hadde ingen systematisk endring ved økt Pauling-elektronegativitet av det sjeldne jordarts kationet. Det ble også observert at aktiveringsenergiene for dekomponeringen hadde en positiv og nesten lineær korrelasjon med kationet sin elektronegativitet. Bragg topper fra ukjente faser dukket opp i mange av prøvene ved oppvarming.

Høy-energisk kulemølling av $NaBH_4$ og $RECl_3$ (*RE* = Tb og Yb) i molforhold 3:1 ble også gjennomført. En ytterligere syntese med $NaBH_4$ og $CeCl_3$ i molforhold 5:3 ble i tillegg utført. Fasesammensetningen og deres krystallstrukturer ble bestemt ved romtemperatur SR-PXD. Syntesene resulterte i dannelsen av de to tidligere urapporterte fasene $NaTb(BH_4)_2Cl_2$ og $NaYb(BH_4)_2Cl_2$. Begge fasene var isostrukturelle med den tidligere rapportert monokliniske fasen $NaY(BH_4)_2Cl_2$ (romgruppe $P2/c$). Prøvene som besto av $TbCl_3$ og $YbCl_3$ inneholdt også Na_3RECl_6 og betydelige mengder av startmaterialene. Store mengder av $CeCl_3$ og en fastløsning av $NaBH_4$ og NaCl ble observert for prøven med $CeCl_3$.

Den termiske stabiliteten og dekomponeringsforløpene av de kloridholdige prøvene ble undersøkt på samme måte som for $Na_2RE_2(BH_4)_5I_3$-fasene. Målingene viste at dekomponeringsforløpet for $NaTb(BH_4)_2Cl_2$ og $NaYb(BH_4)_2Cl_2$ var vesentlig forskjellige. $NaTb(BH_4)_2Cl_2$ dekomponerte i et enkelt steg mens dekoponeringsforløpet for $NaTb(BH_4)_2Cl_2$ besto av flere steg.

Contents

Chapter 1

Introduction

Due to the growing energy consumption in the world and the increasing concern for global warming, discovering new and improved ways to store renewable energy has become an important research topic [1]. Renewable energy can be stored in, for example, batteries or as hydrogen and aim to replace the present use of fossil fuels. Hydrogen gas can be produced from renewable energy by electrolysis of water and has a high energy density, making it an attractive energy carrier. The gas is converted to electricity in a fuel cell where water is the only by-product. A significant challenge in hydrogen technology is the development of effective storage methods [1]. At present, the most common storage method is in high-pressure tanks that can store large quantities of hydrogen gas. However, the energy density in the tanks is not high enough to compete with gasoline or coal [2]. In addition, the compression of the gas requires high energy consumption and comes with many safety concerns. A recent explosion of a hydrogen tank at an Uno-X hydrogen filling station, in the suburbs of Oslo demonstrates the current need for safer hydrogen storage methods [3].

Researchers are currently investigating alternative options for storing hydrogen, such as solid-state hydrogen storage systems. Storing hydrogen in a solid phase enables compact storage and reduces the safety concerns related to leakages and gas at elevated pressures. Lately, metal borohydrides have been examined as possible hydrogen storage materials as they possess high hydrogen densities [4]. Unfortunately, many of the metal borohydrides exhibit poor thermodynamic and kinetic properties, which limit their technical utilization. Alkali and alkaline-earth borohydrides such as $LiBH_4$ and $Mg(BH_4)_2$, have large hydrogen storage capabilities. However, hydrogen release and absorption only occur under severe conditions at elevated temperatures [5, 6]. In contrast, transition metal borohydrides such as $Ti(BH_4)_3$ and $Zr(BH_4)_4$ are too unstable and decompose around room temperature [7, 8]. During recent years, rare-earth borohydrides have been considered as possible hydrogen storage materials [9]. Compounds containing rare-earth metal cations possess a lower gravimetric hydrogen density compared to the alkali and alkaline-earth borohydrides. Nevertheless, the rare-earth borohydrides have a considerable advantage as they have decomposition temperatures between 200 and 300 °C and which is considerably lower compared to $LiBH_4$ which decomposes at 380 °C [9, 5].

Previous research has shown that the stability of the metal borohydrides, in terms of their decomposition temperature, has an inverse correlation with the Pauling electronegativity of the metal cation [10]. This trend is also applicable for the bimetallic borohydrides, where the average electronegativity is used, allowing the possibility to

tune the thermodynamic properties of metal borohydrides. Another method for modifying the thermodynamics is through anion substitution, where the BH_4^- units are partly substituted by halide ions. Examples include $Li(BH_4)_{1-x}Cl_x$ and $Na(BH_4)_{1-x}Cl_x$ [9].

The evolution of batteries has made many advances during the past decade. Lithium-ion batteries (LIBs) are currently dominating the battery market as a result of their high energy density and long cycle life [11]. The conventional battery has a liquid electrolyte, often consisting of organic polymers and have received several safety warnings due to the electrolytes toxicity and flammability [12]. By exchanging the combustible liquid electrolyte with a non-flammable solid-state electrolyte, issues related to fire hazards and leakage can be prevented. The most significant disadvantage of this approach is the notable reduction in ion conductivity, as the ions have reduced mobility in a solid phase [12]. The development of a fast solid-state ion conductor is therefore crucial for the evolution of safe, high energy density batteries.

Investigations related to lithium and sodium ion batteries (SIBs) started simultaneously in the early 1980s. As a result of the successful commercialization of LIBs, there was a considerable reduction in the research related to SIBs [11]. However, solid-state SIBs have recently been regarded as the next generation batteries to replace the current commercial LIBs, with advantages of abundant sodium resources, low cost, and high safety levels. Lithium and sodium are both alkali metals and have similar physical and chemical properties. It is therefore anticipated that SIBs can achieve comparable performance to that of LIBs, in the future [13].

During recent years properties beyond hydrogen storage, such as good ionic conductivity have been observed for some metal borohydrides [1]. It has been suggested that the compounds may be used as active materials in solid-state electrolytes or electrodes, in batteries.

This study is part of a larger effort at the Institute for Energy Technology (IFE) to synthesize and characterize novel alkali conducting materials based on the rare-earth borohydride halides. $LiCe(BH_4)_3Cl$ was the first compound in this class and was found to have high Li-ion conductivity ($0.1\ mScm^{-1}$) at room temperature and a decomposition temperature around 240 °C [14, 15]. The phase was made by ball-milling $LiBH_4$ with $CeCl_3$ in a 3:1 molar ratio. Synthesis with other $RECl_3$ (*RE* = La, Pr, Nd, Sm and Gd) have produced the same phase and the $LiLa(BH_4)_3Cl$ and $LiGd(BH_4)_3Cl$ compounds have even shown higher conductivities, 0.2 and $0.4\ mScm^{-1}$ respectively at room temperature [14].

A new compound, $Na_2La_2(BH_4)_5I_3$ was recently synthesized by ball-milling $NaBH_4$ with LaI_3 [16]. It was later discovered that the same phase could be found for other rare-earth elements such as Ce, Nd, Pr, Gd and Tb [17]. Based on these latest findings, it would be interesting to investigate the thermal properties and decomposition route of the $Na_2RE_2(BH_4)_5I_3$ phase. It is also of interest to examine whether $3\,NaBH_4 + RECl_3$ can yield similar phases of $LiRE(BH_4)_3Cl$ or $Na_2RE_2(BH_4)_5I_3$.

Aim of the work

The goal of this study was to obtain a broader understanding of the rare-earth borohydride halides. The work is a continuation of the Fall 2018 Specialization project, *Synthesis and characterization of sodium rare-earth borohydride halides*. In the previous project samples were synthesized from ball-milling of $NaBH_4$ and REI_3 (*RE* = Y, Ce, Pr, Nd, Gd

and Tb) in a 3:1 molar ratio. Characterization of the as-milled iodide samples at room temperature was conducted and discussed [17]. The present investigation had two main objectives, the first was performing a solid-state synthesis of $NaBH_4$ and $RECl_3$ (*RE* = Ce, Tb and Yb) and characterize the products. The second aim was to determine the phase composition during heating and decomposition behaviour of the iodide and chloride samples, by in-situ powder X-ray diffraction, thermogravimetric analysis, and differential scanning calorimetry.

Chapter 2

Literature review

2.1 Physical and chemical properties of metal borohydrides

Metal borohydrides $M(BH_4)_n$ are compounds where boron and hydrogen form a negatively charged BH_4^- anion, which is counterbalanced by metal cations M^{n+} [4]. The borohydride anion has a tetrahedral structure with a boron atom in the centre and hydrogen atoms in each corner. The B-H bonds are covalent, while the bonds to the cation can either be ionic or covalent. The number of bonded BH_4^- anions to the metal increases with increasing ionic radius of the cation [18]. The bond lengths between the metal and BH_4^- also increase with growing cation radius [19].

Alkaline-earth and transition metal borohydrides are prone to exist as various polymorphs [4]. One extreme example is magnesium borohydride, $Mg(BH_4)_2$ which retains at least seven different polymorphs [20]. This structural flexibility is primarily due to the directionality of the bond between the metal cation and borohydride anion. The degree of directionality in the bond increases with increasing Pauling electronegativity, χ_P, of the metal.

In the case of bimetallic compounds, the most electronegative metal will tend to create a strong covalent bond with the BH_4^- anion, while the less electronegative metal balances out the charge difference [4]. This trend is especially applicable for bimetallic compounds containing an alkali metal, along with an alkaline-earth or transition metal. In these situations, the charge balancing ion will often be the alkali metal [18].

Metal borohydrides have a structural resemblance to metal oxides [19]. The BH_4^- and O^{2-} anions are isoelectronic, both bearing 10 electrons. However, as the negative charge of O^{2-} is twice that of BH_4^-, there will be a higher degree of structural flexibility in the oxides. The two sets of materials also possess similar ionic and covalent characteristics, where the bonding to the cation is partly ionic and partly covalent, making them ionocovalent. This relationship has become especially apparent for the polymorphs of $Mg(BH_4)_2$, where Mg^{2+} and Si^{4+} are isoelectric and the frameworks of the polymorphs resemble different SiO_2 structure types [19].

Halide substitution is an approach to modifying the physical and chemical properties of metal borohydrides, such as hydrogen release or ionic conductivity [21]. During this process, BH_4^- anions are substituted with halide ions, such as Cl^-, Br^- or I^- resulting in a disordered structure. $NaY(BH_4)_{2-x}Cl_{2+x}$ and $LiYb(BH_4)_{4-x}Cl_x$ are examples of metal borohydrides with halide substitution. The BH_4^- anion has an ionic radius of

2.05 $\AA$, while the Cl^- and Br^- ions are slightly smaller with radii of 1.81 and 1.96 $\AA$, respectively [22, 23]. The I^- ion is larger than the $BH_4{}^-$ unit and has an ionic radius of 2.20 $\AA$. The compound containing the smaller anion will often dissolve into the structure of the material consisting of the larger anion resulting in a solid-solution. When the metal borohydride and the metal halide are isostructural, substitution may occur in both compounds, leading to the formation of two solid-solutions. In some cases prolonged heating causes the two solid-solutions to merge into one, and has been observed for $LiBH_4$-LiBr and $NaBH_4$-NaCl systems [4].

2.1.1 Hydrogen storage

Metal borohydrides possess high gravimetric hydrogen densities and have therefore been researched as possible hydrogen storage materials. Examples are $LiBH_4$ and $NaBH_4$ which contain 18.5 wt% and 10.7 wt% hydrogen, respectively [24]. At present, there are no efficient ways of storing large amounts of hydrogen gas. The most utilized storage method is in high-pressure tanks, however, due to their low hydrogen densities and the high energy consumption associated with gas compression, they are not an ideal approach for hydrogen storage [2]. The metal borohydrides such as $LiBH_4$ allow for safe and compact storage of hydrogen gas, with a volumetric hydrogen density of 121 kg H_2 per m^3 [25]. There are still several issues that need to be resolved before the class of materials can be effectively used.

Many of the metal borohydrides possess high kinetic barriers for decomposition and hydrogen adsorption [26]. These processes will, therefore, often occur at elevated temperatures, restricting their technical application. Another concern is the release of diborane gas, B_2H_6 during heating to the hydrogen desorption temperature [26]. Diborane acts as an irritant to skin and eyes and is highly flammable [27]. Metal borohydrides with lower decomposition temperatures tend to release greater amounts of diborane gas [4]. The varying concentrations of hydrogen and diborane in the released gas may be dependent on physical conditions such as hydrogen partial pressure or temperature. It is apparent that certain environments will promote specific reaction paths during desorption.

There are, on the other hand, metal borohydrides that have low thermal stability and decompose around room temperature [9]. Researchers have suggested that the stability of the metal borohydrides is dependent on the charge transfer from the borohydride anion to the metal cation [10]. The decomposition temperature of the compounds decreases with increasing Pauling electronegativity of the metal cation. Borohydrides of metals with electronegativities greater than 1.4 are not suitable for hydrogen storage applications, as they are too unstable.

2.1.2 Ionic conductivity

Some metal borohydrides have displayed good ionic conductivities and may, therefore, have a possible application as solid-state electrolytes in batteries [1]. Solid-state electrolytes have been widely investigated as they remove the safety concerns associated with the toxicity and flammability of liquid electrolytes, found in most batteries used today. Due to the low densities of the metal borohydrides, it is possible to develop lightweight batteries with high concentrations of active material [1].

Many of the metal borohydrides transition to a high-temperature phase upon heating, where the anions shift from an ordered to a disordered state [28]. The high-temperature phase tends to exhibit increased ion mobility, such as for $LiBH_4$ which has a Li-ion conductivity of $10^{-3}\ Scm^{-1}$ for the high-temperature phase (110 °C) and around $10^{-6}\ Scm^{-1}$ at room temperature [1]. Figure 2.1 depicts the phase transition for $LiBH_4$, occurring at around 380-390 K. This implies that the phase transition temperature must be lowered for it to be possible to attain high ionic conductivity at room temperature. So far this has been achieved by partially substituting the BH_4^- anions with halide anions, creating a solid-solution [28].

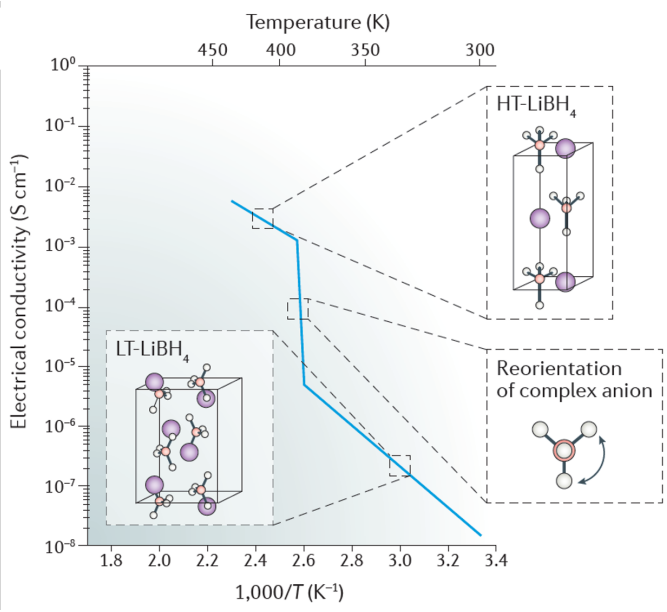

Figure 2.1: Arrhenius plot showing the ionic conductivity of $LiBH_4$ during heating. The figure exhibits the phase transition from the low-temperature (LT) to the high-temperature (HT) phase, taken from Ref. [4].

2.2 Thermodynamic and kinetic properties of metal borohydrides

Metal borohydrides possess high gravimetric and volumetric hydrogen densities. However, mechanisms relating to hydrogen release or absorption have shown to have high kinetic barriers, resulting in the mechanisms only occurring at elevated temperatures [29]. Stable monometallic borohydrides often melt before decomposition at slightly higher temperatures, while unstable compounds tend to decompose instantly in the gas phase. Stable monometallic borohydrides typically decompose into compounds such as metal boranes, metal hydrides or metal borides. The decomposition products tend to be non-crystalline, and characterization techniques such as ^{11}B NMR are useful for identifying the amorphous phases [4].

A correlation between the decomposition temperature, T_{dec} and the Pauling electronegativity of the cation has been observed for the more stable metal borohydrides [10]. The decomposition temperature will decrease almost linearly with increasing Pauling electronegativity of the metal cation as illustrated by the red line in Figure 2.2. Deviations from this linear behaviour have been found for compounds consisting

of metals with higher electronegativities. An exponential correlation between the decomposition temperature and the electronegativity of the metal has been proposed for the latter (blue curve in Figure 2.2) [9]. As seen in the figure, rare-earth borohydrides such as $Gd(BH_4)_3$ and $Y(BH_4)_3$ have decomposition temperatures of around 200-300 °C. Their thermal stability lies between that of alkali metal borohydrides and transition metal borohydrides, and they have therefore been considered as possible hydrogen storage materials.

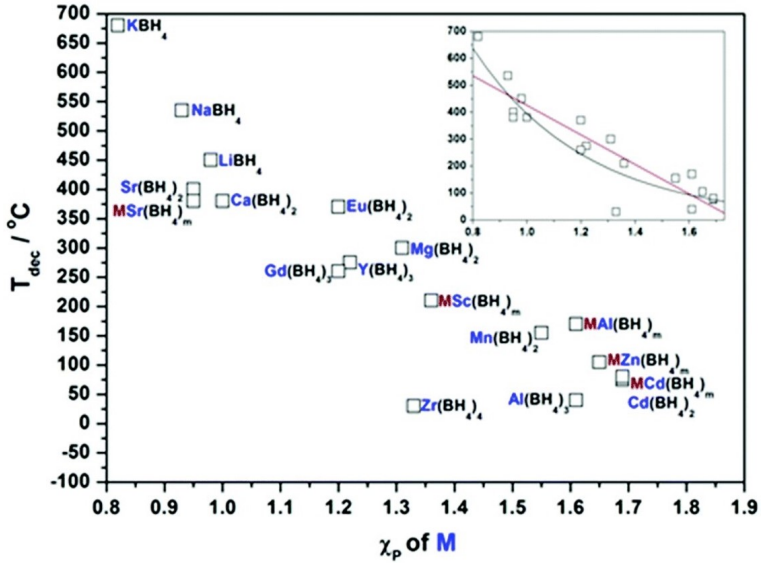

Figure 2.2: Decomposition temperature of various metal borohydrides as a function of the electronegativity of the central metal cation, taken from Ref. [4]. The figure also displays a comparison of the linear and exponential correlation between the two.

2.3 Synthesis of rare-earth borohydrides

The most common synthesis routes for *RE* borohydrides (*RE* = rare-earth) are mechanochemistry and solvent-based methods [4]. High energy ball-milling is a popular mechanochemistry method and involves a metathesis reaction between the reactants, such as a rare-earth chloride and an alkali metal borohydride [9]. Reactions are activated by the impacts between the milling medium and the grains, providing energy and producing new and reactive surfaces. Lithium borohydride has demonstrated to be an effective precursor for these types of reactions. When mixtures of trivalent *RE* chloride and $LiBH_4$ undergo a metathesis reaction, the outcome can either be the formation of a monometallic, bimetallic or chloride containing *RE* borohydride, as shown by Equations (2.1) - (2.3):

$$RECl_3 + 3LiBH_4 \rightarrow RE(BH_4)_3 + 3LiCl \tag{2.1}$$

$$RECl_3 + 4LiBH_4 \rightarrow LiRE(BH_4)_4 + 3LiCl \tag{2.2}$$

$$RECl_3 + 3LiBH_4 \rightarrow LiRE(BH_4)_3Cl + 2LiCl \tag{2.3}$$

A considerable disadvantage of ball-milling is the limited control of the reaction conditions during synthesis [9]. The milled sample will consist of the metal borohydride and the metal halide if the synthesis is successful. The metal halide phase is generally unwanted and could potentially influence the chemical and physical properties of the sample. After ball-milling, the sample will often have low crystallinity, and additional heat treatment is required for analysis by powder X-ray diffraction. The heat treatment needs to be conducted carefully to prevent the decomposition of the material.

Solvent-based methods are in some cases preferred over ball-milling, as it is easier to separate the metal borohydrides from the by-products, hence obtaining a pure phase sample. An example is a reaction between a metal hydride and a borane donor anion, where a solvated metal borohydride complex is formed, as displayed in Equation 2.4. [30]. A reaction between an alkali borohydride and a metal chloride conducted with an organic solvent will also yield a metal borohydride product. Both reactions require further heat treatment to remove the solvents (Equation 2.5), thus introducing the risk of decomposition during solvent removal.

$$REH_3(s) + 3S(CH_3)_2 \cdot BH_3(l) \rightarrow RE(BH_4)_3 \cdot (CH_3)_2(s) + 2S(CH_3)_2(l) \tag{2.4}$$

$$RE(BH_4)_3 \cdot S(CH_3)_2(s) \rightarrow RE(BH_4)_3(s) + S(CH_3)_2(g) \tag{2.5}$$

2.4 Prior studies of rare-earth borohydrides

Rare-earth borohydrides are often classified into four groups, mono-, bi-, and trimetallic and halide-containing *RE* borohydrides [9]. The momometallic *RE* borohydrids can be sub-grouped into distorted ReO_3-type (α-*RE*$(BH_4)_3$), ReO_3-type (β-*RE*$(BH_4)_3$) and alkaline-earth borohydride-type (*RE*$(BH_4)_2$). Table 2.1 gives an overview of some of the many reported *RE* borohydrides.

Table 2.1: An overview of some of the reported rare-earth borohydrides.

RE^{3+}	ion radius [Å][23]	α-*RE*$(BH_4)_3$ (Cubic)	β-*RE*$(BH_4)_3$ (Cubic)	Li*RE*$(BH_4)_4$ (Tetragonal)	Na*RE*$(BH_4)_4$ (Orthorhomic)	Li*RE*$(BH_4)_3$Cl (Cubic)	$Na_2RE_2(BH_4)_5I_3$ (Monoclinic)
Sc^{3+}	0.885			X[31]	X[32]		
Y^{3+}	1.04	X[33]	X[34]	X[35]	X[35]		
La^{3+}	1.172				X[36]	X[37]	X[16]
Ce^{3+}	1.15	X[30]	X[38]		X[39]	X[29]	X[17]
Pr^{3+}	1.13	X[40]	X[39,40]		X[39]	X[29]	X[17]
Nd^{3+}	1.123	X[40]	X[40]			X[29]	X[17]
Sm^{3+}	1.098	X[29]	X[29]			X[29]	
Gd^{3+}	1.078	X[33]				X[37]	X[17]
Tb^{3+}	1.063	X[29]					X[17]
Dy^{3+}	1.052	X[33]					
Ho^{3+}	1.041	X[41]	X[41]				
Er^{3+}	1.03	X[39]	X[29]		X[39]		
Tm^{3+}	1.03	X[19]					
Yb^{3+}	1.008	X[29]	X[29]	X[42]	X[43]		
Lu^{3+}	1.001	X[30]	X[30]		X[29]		

2.4.1 Lithium rare-earth borohydrides

There are so far four different structures reported for *RE* borohydride phases prepared by mechanochemical reactions of $LiBH_4$ with $RECl_3$ [9]. These phases are: Li*RE*$(BH_4)_4$, α-*RE*$(BH_4)_3$, β-*RE*$(BH_4)_3$ and Li*RE*$(BH_4)_3Cl$.

As stated in the introduction the first *RE* borohydride halide was $LiCe(BH_4)_3Cl$ [14]. The compound has a body-centered cubic structure with space group $I\bar{4}3m$ an ionic conductivity of $0.1\ mScm^{-1}$. The phase can be formed by other large *RE* elements such as La, Pr, Nd, Sm and Gd (Equation 2.3) [29, 37]. Furthermore the $LiLa(BH_4)_3Cl$ and $LiGd(BH_4)_3Cl$ phases have higher conductivities, 0.2 and $0.4\ mScm^{-1}$ respectively at room temperature [14]. Reacting $LiBH_4$ with LaX_3 (X = Br and I) has resulted in producing phases with the same structure, $LiLa(BH_4)_3X$ [39].

α-*RE*$(BH_4)_3$ has a distorted ReO_3-type structure with space group $Pa\bar{3}$ [29]. This phase has been reported for the majority of the *RE* elements (Figure 2.1). α-*RE*$(BH_4)_3$ transforms into a high-temperature phase, β-*RE*$(BH_4)_3$ when annealed at around 199-488 °C, depending on the type of *RE* cation [4]. The phase has a regular ReO_3-type structure and can display either a primitive cubic ($Pm\bar{3}m$) or a face-centered cubic ($Fm3c$) unit cell, depending on if the BH_4^- units have a disordered or ordered orientation, respectively. The $Fm3c$ space group has been reported for *RE* = Y, Ce, Pr, Nd, Sm, Ho, Er, Yb and Lu, while the $Pm\bar{3}m$ space group has been reported for *RE* = Pr, Sm, and Yb [29, 30, 34, 38, 39, 40, 41]. Distinguishing the two structures by use of X-ray diffraction is difficult, as the light hydrogen atoms have little effect on the diffraction pattern compared to the much heavier rare-earth metals. The structures can be differentiated by neutron diffraction. However, this technique is expensive, due to the high costs of building and maintaining a neutron source and the need for costly isotopes (^{11}B and D) [44].

The Li*RE*$(BH_4)_4$ phase has a tetragonal ($P\bar{4}2c$) unit cell and is reported for *RE* = Sc, Y, Er and Yb [31, 35, 42]. The $LiY(BH_4)_4$ compound has shown low ionic conductivity, $1.26\ \ 10^{-3}\ mScm^{-1}$ at room temperature [35].

2.4.2 Sodium rare-earth borohydrides

There are considerably fewer reports of sodium *RE* borohydrides compared to lithium *RE* borohydrides. Most sodium *RE* borohydrides are found as bimetallic borohydrides, such as Na*RE*$(BH_4)_4$ which has an orthorhombic structure with either a $Pbcn$ or $Cmcm$ space group. The phase can be synthesized by ball-milling or through solvent-based methods [39]. The $Pbcn$ space group has been observed for *RE* = La, Ce and Pr while the $Cmcm$ space group is reported for *RE* = Sc, Y, Er and Yb [29, 32, 35, 36, 39, 43]. The $NaY(BH_4)_4$ phase has demonstrated Na-ion conductivity, however only at very low levels ($6.92\ x\ 10^{-4}\ mScm^{-1}$ at RT) [35].

Na*RE*$(BH_4)Cl$ is a mixed-cation mixed-anion borohydride [45]. The phase has a monoclinic structure with space group $P2/c$ and was synthesized through ball-milling of $NaBH_4$ and YCl_3 and subsequent annealing. Yttrium is the only *RE* element that has produced this phase so far.

Researchers at the Institute for Energy Technology recently synthesized a new compound from the mechanochemical reaction between $NaBH_4$ and LaI_3 (Equation 2.6) [16]. From the reaction the $Na_2La_2(BH_4)_5I_3$ phase was obtained together with a solid-solution of $NaBH_4$ and NaI. The phase has a monoclinic structure with space group

$C2/m$ (Figure 2.3). It has been speculated if the large structure allows for Na-ion mobility, thus possibly giving the compound an application as a solid-state electrolyte in sodium batteries.

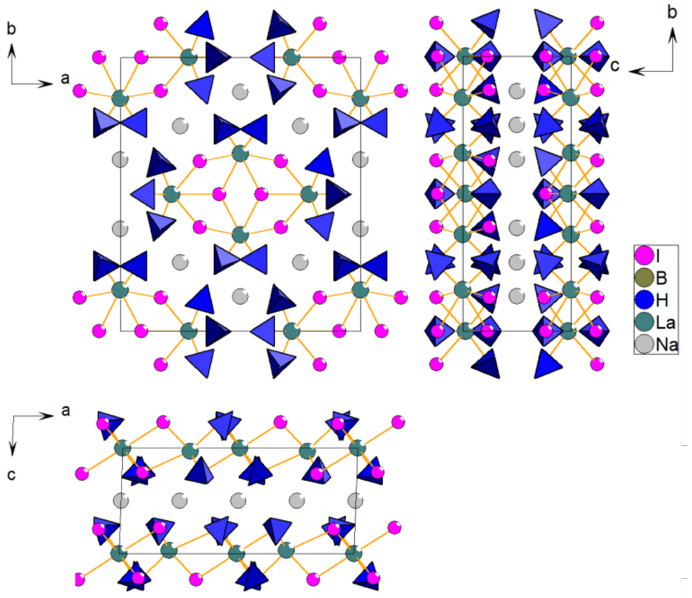

Figure 2.3: Crystal structure of the $Na_2La_2(BH_4)_5I_3$ compound [16].

A recent study showed that the $Na_2RE_2(BH_4)_5I_3$ compound can also be observed for *RE* = Ce, Pr, Nd, Gd and Tb [17]. The compounds were synthesized by ball-milling $NaBH_4$ and REI_3 in a 3:1 molar ratio. Table 2.2 gives and overview of the phases found in each sample, *Na-RE-I* (*RE* = Y, Ce, Pr, Nd, Gd, Tb and Er) in the study. The as-milled samples containing REI_3 (*RE* = Ce, Pr and Nd) followed the reaction given in Equation 2.6. A balanced reaction for the samples comprising of two solid-solutions, *Na-Gd-I* and *Na-Tb-I* was unfortunately not found. It was further reported that the weight fraction of $Na_2RE_2(BH_4)_5I_3$ in the samples decreased down the rare-earth series, with the Ce sample having the highest weight fraction and Tb the lowest. It was also observed that the samples synthesized from the orthorhombic iodides, REI_3 (*RE* = Ce, Pr and Nd) resulted in $Na_2RE_2(BH_4)_5I_3$ while the samples ball-milled from the tetragonal iodides, GdI_3 and TbI_3 contained both $Na_2RE_2(BH_4)_5I_3$ and α-$RE(BH_4)_3$. Ball-milling of the the tetragonal iodides, YI_3 and ErI_3 resulted only in the formation of the α-$RE(BH_4)_3$ phase, following the reaction given in Equation 2.7. Both *Na-Gd-I* and *Na-Er-I* contained an oxidized phase, which could be due to contamination of the starting materials, $NaBH_4$ and REI_3 or by inadequate sealing of the capillaries during PXD measurements. All the samples contained a solid-solution of NaI and $NaBH_4$, while many of the samples also had significant amounts of REI_3 after ball-milling. It was therefore concluded that reactions were not successfully completed.

$$(5+x)NaBH_4 + 2REI_3 \rightarrow Na_2RE_2\left(BH_4\right)_5 I_3 + (3+x)Na\left(BH_4\right)_{\left(\frac{x}{3+x}\right)} I_{\left(\frac{3}{3+x}\right)} \tag{2.6}$$

$$(3+x)NaBH_4 + REI_3 \rightarrow \alpha - RE(BH_4)_3 + (3+x)Na\left(BH_4\right)_{\left(\frac{x}{3+x}\right)} I_{\left(\frac{3}{3+x}\right)} \tag{2.7}$$

Table 2.2: Overview of qualitative amounts, X (trace), XX (moderate amount) and XXX (main phase), of each phases observed in the *Na-RE-I* samples [17].

	Na-Y-I	*Na-Ce-I*	*Na-Pr-I*	*Na-Nd-I*	*Na-Gd-I*	*Na-Tb-I*	*Na-Er-I*
$Na_2RE_2(BH_4)_5I_3$		XXX	XXX	XXX	X	X	
α-$RE(BH_4)_3$	XX				X	XX	XXX
$Na(BH_4)_{1-x}I_x$ (NaI rich)	XXX	XXX	XXX	XX	XX	XX	XXX
$Na(BH_4)_{1-x}I_x$ ($NaBH_4$ rich)					XXX	XXX	
REI_3			XX	XXX	XXX	X	
*RE*OI					X		X

The *Na-Ce-I* sample contained the largest amount of $Na_2RE_2(BH_4)_5I_3$ with the fewest by-products [17]. The Rietveld refinement of the sample at room temperature is displayed in Figure 2.4, where both the $Na_2Ce_2(BH_4)_5I_3$ and NaI phases are included. The weighted *R*-factor of the refinement was 6.779, indicating a good match with the measured data. The weight fractions of $Na_2Ce_2(BH_4)_5I_3$ and NaI were 0.480 and 0.520 respectively.

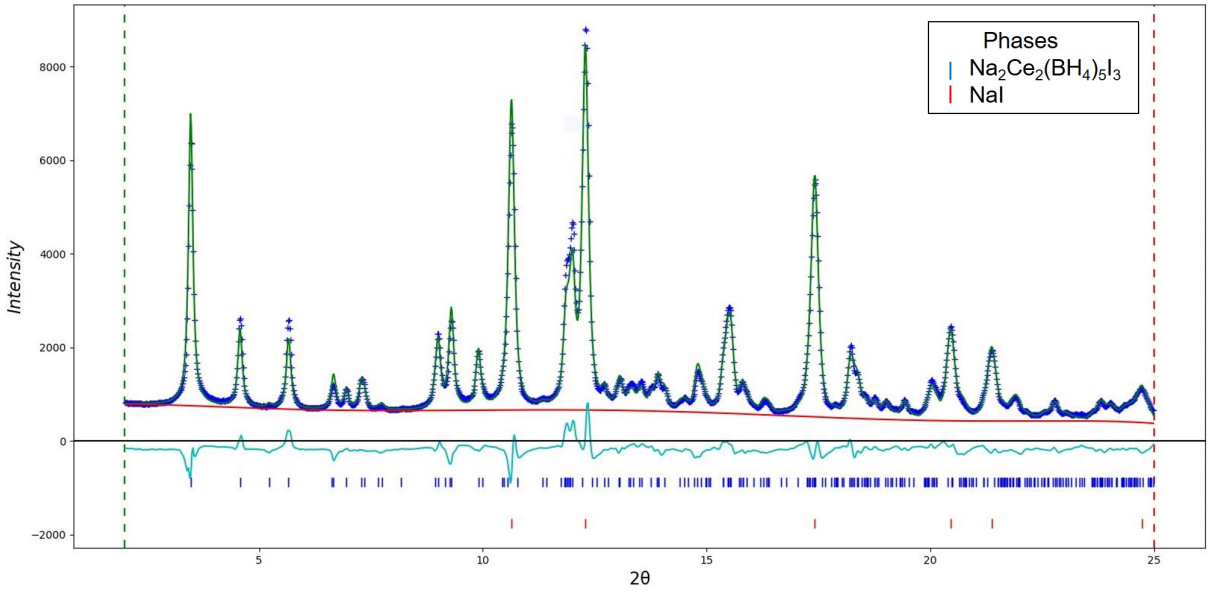

Figure 2.4: Rietveld refinement of *Na-Ce-I*, where the blue crosses in the diffraction patterns indicate the observed data (Y^{obs}), while the green line is the calculated profile (Y^{calc}). The red line is the fitted background ($Y^{background}$) and the turquoise line is the difference in intensity between the observed data and the fitted profile ($Y^{obs} - Y^{calc}$) [17].

2.4.3 Stability of rare-earth borohydrides

The Pauling electronegativity of the *RE* elements ranges from 1.10 for Lanthanum to 1.27 for Lutetium [44]. Due to this narrow gap, the variation in decomposition temperatures is far less pronounced in the *RE* borohydrides in comparison to the alkali or alkaline-earth borohydrides. The decomposition for the monometallic trivalent *RE* borohydrides, such as α, and β-$RE(BH_4)_3$ tend to result in the formation of the corresponding rare-earth hydrides and borides (Equation 2.8) [46]. The decomposition

route of larger compounds such as Li*RE*$(BH_4)_3Cl$ appears to be more complex, often involving multiple steps.

$$\alpha\text{-Er}(BH_4)_3 = 0.75ErB_4 + 0.25ErH_2 + 5.75H_2 \tag{2.8}$$

It is difficult to establish trends in the thermal decomposition of the *RE* borohydrides. The main reason for this is the use of different preparation methods [9]. An example is the decomposition of α-Tb$(BH_4)_3$. A phase pure α-Tb$(BH_4)_3$ sample synthesized by a solvent-based method undergoes a single step decomposition at 275 °C, while a sample synthesized by ball-milling undergoes a two-step decomposition in the temperature range of 201-250 °C [29, 30]. In this example the ball-milled sample was synthesized from a 3:1 mixture of $LiBH_4$ and $TbCl_3$ and the sample consisted of α-Tb$(BH_4)_3$, LiCl and $LiBH_4$. It is, therefore, apparent that the presence of by-products lowers the decomposition temperature of the *RE* borohydride. This can be due to the by-products acting as catalysts promoting decomposition or that a reaction between the by-products and *RE* borohydride occurs.

2.5 X-ray diffraction

X-rays are electromagnetic radiation with wavelengths of 0.01 to 10 nm and are generated when charged particles such as electrons are accelerated through several kV and collide with a metal anode, e.g. copper [47]. The impact causes a 1s (K-shell) electron to be knocked out from the Cu atom, and an electron from an outer orbital (2p or 3p) will immediately occupy the vacancy. When the outer electron drops down to the 1s level, energy is released in the form of X-ray radiation. Each element has a range of transition energies that correspond to a type of transition. For instance, a transition from 2p to 1s is called K_α and has a wavelength of 1.5418 $\AA$ for Cu, while a transition from 3p to 1s is denoted as K_β. For a Cu atom the K_β transition will have a wavelength of 1.3922 $\AA$ [44]. K_α radiation has a higher intensity compared to K_β because the transition occurs more frequently. As a result of the 2p electrons having two possible spin states with marginally different energies, the K_α radiation is a doublet, having values of $K_{\alpha1}$ = 1.54051 $\AA$ and $K_{\alpha2}$ = 1.54433 $\AA$ for copper [44].

An X-ray diffractometer (Figure 2.5) consists of an X-ray tube and an X-ray detector, which are attached to two separate mechanical arms that are mounted on a goniometer [44]. The sample is placed in the centre of the goniometer axis, and the arms are free to rotate in either direction or stay stationary in one position. The X-ray tube consists of a tungsten filament and an anode with a fixed metal target at the end, often Cu. The filament emits a beam of accelerated electrons that strike the target, causing some of the metal atoms to ionize and subsequently emit X-ray radiation. The anode needs continuous cooling as the majority of the energy from the electrons is converted to heat. The K_α radiation is used for diffraction, while the weaker K_β radiation is removed, resulting in a monochromatic beam of X-rays. The K_β radiation can be removed by a monochromator, a *Göbel* mirror or by other optical methods. Another approach for removal is using nickel foil, which absorbs the K_β radiation.

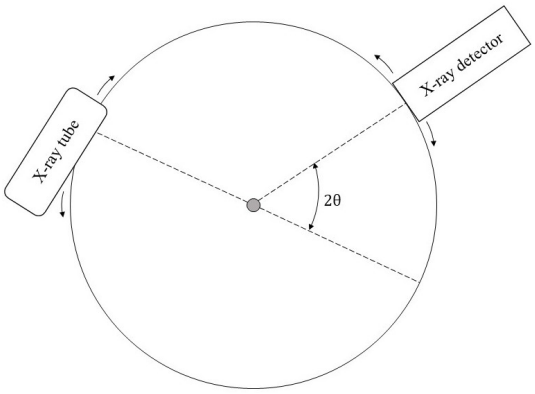

Figure 2.5: Schematic diagram of an X-ray diffractometer.

Crystalline materials are compounds with atoms arranged in a repeating or periodic array over large atomic distances. When X-rays encounter the atomic planes of a crystal, the radiation is scattered and interfere with one another as they leave the crystal [48]. Constructive interference, i.e. the reflected beams are in-phase will occur when the conditions of Bragg's law are fulfilled (Equation 2.9) [47]. In the equation, λ is the wavelength of the X-rays, and θ is the scattering angle. d_{hkl} is the interplanar spacing, where the subscripts hkl are the Miller indices of the atomic plane.

$$\lambda = 2d_{hkl}sin\theta \tag{2.9}$$

2.5.1 Powder X-ray diffraction

Powder X-ray diffraction (PXD) is the most common technique for identifying crystalline phases in a material [47]. The method can be used to determine the lattice parameters and atomic positioning of a compound. A powder sample is polycrystalline as it contains numerous small crystallites with random orientation [44]. When X-rays radiate a polycrystalline material, the radiation is scattered, following Bragg's law. It is assumed that a large number of the crystallites must have lattice planes oriented at the Bragg angle, 2θ. Powder samples are often rotated during measurement, as it enhances the number of crystallites that contribute to diffraction. The resulting scattering is a cone often referred to as Debye-Scherrer rings (Figure 2.6) [44].

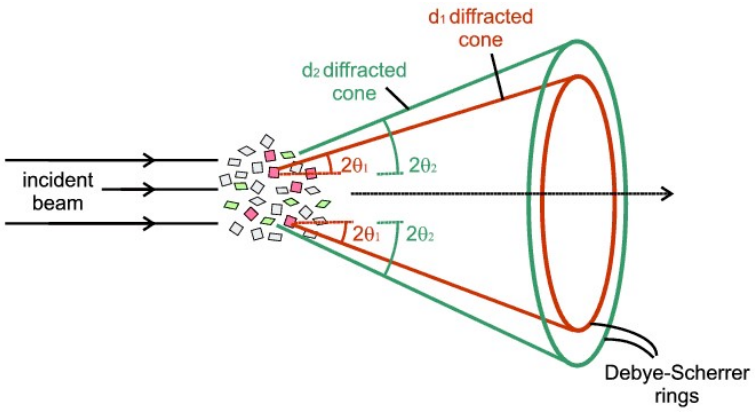

Figure 2.6: Formation of Debye-Scherrer rings by powder X-ray diffraction. Figure taken from Ref. [49].

Diffraction patterns are useful for phase identification because every crystalline solid has a unique pattern, which may be used as a "fingerprint" for the phase [47]. A diffraction pattern contains Bragg reflections at certain 2θ angles with specific intensities, measured with a fixed wavelength. The positions of the reflections express the lattice spacing in the unit cell, while the intensities provide information about the atomic arrangement. The intensity of a reflection, Y_{hkl} is proportional to the squared structure factor, $|F_{hkl}|^2$ as shown in Equation 2.10 [44]. In the equation, f_j is the atomic scattering factor for any atom j in the unit cell, h, k and l are the Miller indices of the scattering plane and x_j, y_j and z_j are the coordinates of atom j. The summation is over all the atoms in the unit cell. If the atomic coordinates in a unit cell are known, the equation can be used to determine the intensity of any reflection. This relationship is applied in the Rietveld method, which is later presented in Section 2.5.3.

$$Y_{hkl} \propto |F_{hkl}|^2 = |\sum_j f_j exp\left(2\pi i\left(hx_j + ky_j + lz_j\right)\right)|^2 \tag{2.10}$$

Vegard's law

When two solids have the same crystal structure and atoms of approximately the same size, they can dissolve into one another, forming a solid solution. The unit cell parameters of a solid solution have a linear correlation with the phase composition, as established by Vegard's law [48]. Vegard's law is given in Equation 2.11 where a_1 and a_2 are the lattice parameters of *Solid 1* and *Solid 2* respectively, a_{ss} is the lattice parameter of the solid-solution and x_2 is the mole fraction of *solid 2* in the solid-solution. The equation illustrates that as the amount of *solid 2* increases, the lattice parameter of the solid-solution will increase accordingly. The law portrays an ideal system, and therefore it is not uncommon for experimental measurements to deviate from linearity. Points above the ideal line are said to show a positive deviation, while points below display a negative deviation (Figure 2.7) [48].

$$x_2 = \frac{a_{ss} - a_1}{a_2 - a_1} \tag{2.11}$$

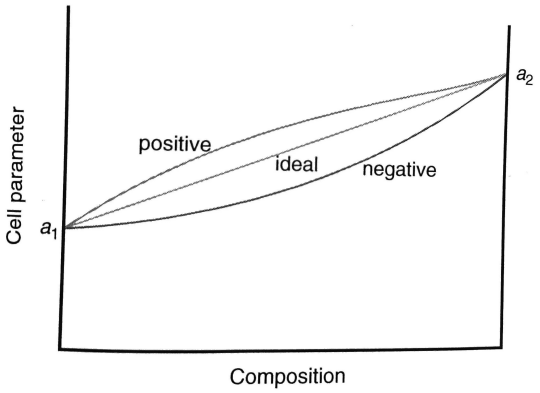

Figure 2.7: Relationship between unit cell parameters and composition in accordance to Vegard's law. Figure taken from Ref. [48].

2.5.2 Synchrotron radiation

An alternative method to produce X-rays is in large synchrotron facilities. In such facilities, electrons are accelerated to velocities close to that of light and injected into a synchrotron storage ring [44]. The ring has a diameter up to several hundreds of meters and consists of both straight and curved sections, with multiple bending magnets spread along the track at the curved segments (Figure 2.8). The magnets generate magnetic fields that force the electrons to change direction, producing a stream of synchrotron radiation, tangential to the electron path. The linear segments are fitted with insertion devices known as wigglers or undulators. These devices emit magnetic fields perpendicular to the storage ring and cause electron deflection in the horizontal plane. Due to the contribution of multiple magnetic dipoles in the insertion devices, the radiation emitted is more powerful than the radiation produced by the bending magnets. The radiation from the bending magnets and insertion devices are directed towards various beamline hutches located along the storage ring.

The radiation can have a wide range of wavelengths and will vary between synchrotrons and beamlines depending on the energy of the electrons and the curvature of their path [44]. Everything from radio frequencies to gamma-rays can be produced, and a wide variety of diffraction and spectroscopic instruments can, therefore, be employed. Synchrotron radiation can produce high-intensity X-ray beams that can be used for powder diffraction. This technique is called synchrotron radiation powder X-ray diffraction (SR-PXD) and can produce high-quality powder diffraction data with respect to intensity and resolution.

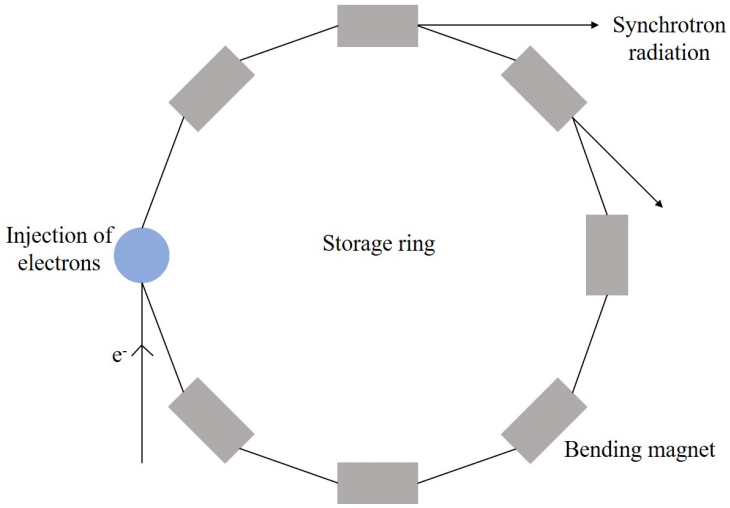

Figure 2.8: Simple illustration of a synchrotron storage ring [44].

2.5.3 Rietveld refinement

The Rietveld method is a structural refinement technique that is used to evaluate diffraction patterns [50]. The method was initially developed for neutron powder diffraction but has later been applied to powder X-ray diffraction [44]. A non-linear least squared minimization of function, M is used to fit a calculated profile from a model to a measured pattern (Equation 2.12) [50]. In the equation Y_i^{obs} and Y_i^{calc} are the observed and calculated intensities at point i in the pattern respectively, while $\sigma_{M_i}^2$ is the standard deviation of Y_i^{obs}.

$$M = \sum_{i=1}^{N} \frac{1}{\sigma^2_{Y_i^{obs}}} \left(Y_i^{obs} - Y_i^{calc}\right)^2 \tag{2.12}$$

The diffraction pattern of the model is calculated by use of Equation 2.13, where S is the scaling factor, m_{hkl} is a multiplicity factor, L_{hkl} is the Lorentz factor, P_{hkl} is a polarization factor, A_i is an absorption coefficient, F_{hkl} is a structure factor and $f(2\theta_i^{hkl})$ is the profile function [50]. The subscripts *hkl* are the Miller indices of the Bragg reflections that contribute to the intensity in the measured point i. Y_i^{bkg} is the background intensity of a point i in the pattern. The background is a polynomial often given a Chebyshev function.

$$Y_i^{calc} = S \sum_{hkl} m_{hkl} L_{hkl} P_{hkl} A_i |F_{hkl}|^2 f\left(2\theta_i^{hkl}\right) + Y_i^{bkg} \tag{2.13}$$

The profile function, $f(2\theta_i^{hkl})$ is usually a linear combination of a normalized Gaussian- and normalized Lorentzian function, denoted as a Pseudo-Voigt function [50]. The Gaussian and Lorentzian contributions are shown in Equations 2.14 and 2.15 respectively. In the equations, H_{hkl} and Γ_{hkl} are the Gaussian and Lorentzian full-width at half-maximum (FWHM) respectively of the peak. G_U, G_V and G_U are refinable parameters for the Gaussian peak profile, while L_X and L_Y are refinable parameters that correlate to the crystal strain and size respectively. $2\theta_i^{hkl}$ is the Bragg angle for the atomic plane with Miller indices *hkl* at point i in the pattern.

$$H_{hkl} = \sqrt{G_U \tan^2\left(2\theta_i^{hkl}\right) + G_V \tan\left(2\theta_i^{hkl}\right) + G_W} \tag{2.14}$$

$$\Gamma_{hkl} = L_X \tan\left(2\theta_i^{hkl}\right) + \frac{1}{\cos\left(2\theta_i^{hkl}\right)} L_Y \tag{2.15}$$

A Rietveld refinement aims to refine the different parameters so that Y_i^{obs} is as close to Y_i^{calc} as possible. An indicator that can be used to determine the agreement between the data and model is the weighted profile *R*-factor, R_{wp} [50]. If the calculated profile is a good fit with the experimental data, a low *R*-factor is given.

$$R_{wp} = \sqrt{\frac{\sum_{i=1}^{N} \frac{1}{\sigma^2_{Y_i^{obs}}} \left(Y_i^{obs} - Y_i^{calc}\right)^2}{\sum_{i=1}^{N} \frac{1}{\sigma^2_{Y_i^{obs}}} \left(Y_i^{obs}\right)^2}} \tag{2.16}$$

2.5.4 Pawley refinement

The Pawley method was developed by Pawley in 1981 and is often conducted if the structure of a phase is unknown [51]. The Pawley and Rietveld methods are closely related, wherein both methods the position of the reflections are determined by the unit cell parameters and space group of the refined phases. However, in a Pawley refinement, the intensities the Bragg peaks are independent variables, while in a Rietveld refinement, the intensities are determined by the atomic structure from the structure factor. Equation 2.13 can, therefore, be rewritten as Equation 2.17, where the multiplicity, polarization, absorption and structure factors are all gathered into one independent variable, I_{hkl}. In the equation, I_{hkl} is the intensity of each reflection with Miller indices,

hkl [51]. Like the Rietveld refinement the weighted profile *R*-factor, R_{wp} is used as an indication of how well the calculated profile fits with the experimental data.

$$Y_i^{calc} = S \sum_{hkl} I_{hkl} f\left(2\theta_i^{hkl}\right) + Y_i^{background} \tag{2.17}$$

2.6 Thermal Analysis

Thermal analysis involves the investigation of different physical and chemical properties of a material, as a function of temperature [44]. Two of the most commonly used thermal analysis techniques are thermogravimetric analysis (TGA) and differential scanning calorimetry (DSC).

2.6.1 TGA and DSC

A TGA measures the change in mass as a function of temperature or time, while a DSC measurement shows the change in enthalpy [44]. Since heating of the sample is required in both TGA and DSC, a simultaneous instrument setup is often used (Figure 2.9). The setup consists of two identical crucibles placed on a pedestal that is mounted to a balance. The sample is placed in the left crucible while the right crucible is empty and used as a reference. Two separate thermocouples are situated underneath the crucibles, allowing the temperature of the sample (T_S) and reference (T_R) to be monitored. A cylindrical oven is lowered, enclosing the system and inert gas is flowed through the system, as indicated by the arrows in Figure 2.9.

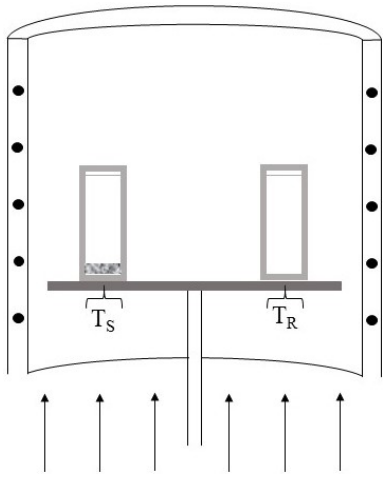

Figure 2.9: Depiction of the simultaneous TGA and DSC apparatus.

The sample is heated at a constant rate, and a change in the mass is due to the uptake or release of gases [44]. The change in enthalpy is monitored by the difference in the heat flux between the sample and the reference. A positive peak in the DSC reading relates to an endothermic reaction in the sample, while a negative peak expresses an exothermic reaction. An endothermic peak combined with a weight loss indicates a decomposition reaction. A phase transition, solid-state reaction or melting is expressed by an endothermic peak with no weight loss. Exothermic signals upon heating sug-

gest that non-equilibrium reactions, such as crystallization or reactions of metastable phases are taking place.

2.6.2 The Kissinger analysis

The Kissinger equation can be used to determine the energy barriers for chemical and physical transformations, such as crystallization and decomposition [52]. The temperature at which the transformation rate is at its maximum is often referred to as the peak temperature. By assuming the transformation is controlled by a single mechanism the transformation rate, $\frac{d\alpha}{dt}$ can be expressed by Equation 2.18, where t is time, $f(\alpha)$ is the conversion function, α is the degree of transformation ($0 < \alpha < 1$), A is a constant, E_a is the activation energy, R is the universal gas constant and T is the temperature [52].

$$\frac{d\alpha}{dt} = f(\alpha)\ Aexp\left(-\frac{E_a}{RT}\right) \tag{2.18}$$

If continuous heating conditions ($\beta = dT/dt$) are used Equation 2.18 can be rewritten as Equation 2.19.

$$\frac{d\alpha}{dT} = \frac{1}{\beta} f(\alpha)\ Aexp\left(-\frac{E_a}{RT}\right) \tag{2.19}$$

By setting the first derivative of the transformation rate to equal zero the *Kissinger equation* can derived (Equation 2.20). In the equation T_M is the peak temperature while α_M is the degree of transformation at T_M. From the *Kissinger equation* the activation energy can be obtained by performing a linear regression of the plot $ln(\beta_i/T_{M,i}^2)$ versus $1/T_{M,i}$. The method is however only an approximation as it assumes that the last term on the right-hand side is independent of the heating rate, β [52].

$$ln\left(\frac{\beta}{T_M^2}\right) = -\frac{E_a}{RT_M} + ln\left(-\frac{AR}{E_a} f'(\alpha_m)\right) \tag{2.20}$$

Chapter 3

Experimental

For this investigation three samples were prepared from anhydrous sodium borohydride, $NaBH_4$ and rare-earth chloride, $RECl_3$ (*RE* = Ce, Tb and Yb). In-situ synchrotron radiation powder X-ray diffraction (SR-PXD) and simultaneous TGA and DSC measurements were conducted on the newly synthesized chloride samples and the iodide samples that were prepared during Fall of 2018 [17]. An overview of the initial sample compositions of the iodide samples are presented in Tables A.2 and A.3 in Appendix A.

3.1 Synthesis of materials

3.1.1 Sample preparation

Three samples were prepared and held under argon atmosphere inside an MBraun Unilab glove-box. Two of the samples were mixed in a 3:1 molar ratio of, $NaBH_4$ and $RECl_3$ (*RE* = Tb and Yb). The last sample consisted of a 5:3 molar ratio of $NaBH_4$ and $CeCl_3$ [1]. The samples were given abbreviated names, as shown in Table 3.1. The *RE* chlorides had different crystal structures, and these are also presented in the table below. The exact sample compositions are given in Table A.1 in Appendix A.

Table 3.1: The abbreviated names and the initial composition of the samples, together with the crystal structures of the various rare-earth chlorides.

Sample	Initial composition	Structure of $RECl_3$
Na-Ce-Cl	$5NaBH_4 + 3CeCl_3$	Hexagonal ($P63/m$)
Na-Tb-Cl	$3NaBH_4 + TbCl_3$	Orthorhombic ($Cmcm$)
Na-Yb-Cl	$3NaBH_4 + YbCl_3$	Monoclinic ($C2/m$)

3.1.2 Ball-milling

A Fritsch Pulverisette 6 ball-mill (Figure 3.1) and a 30:1 ball-to-powder mass ratio of stainless steel balls were used to mill the samples. The reactants were added to the ball-mill crucible and sealed shut while inside the glove-box. The powders were set to 15 minutes milling at 500 rpm with 5-minute pauses. This interval was repeated 17

[1] A sample with a 3:1 molar ratio of $NaBH_4$ and $CeCl_3$ has been attempted before and showed no Bragg reflections from unreported phases. A synthesis using a new molar ratio was therefore attempted.

times, hence the total milling time for one sample was 6 hours. After milling the sealed crucible was brought back into the glove-box, and the samples were transferred and stored in small glass jars.

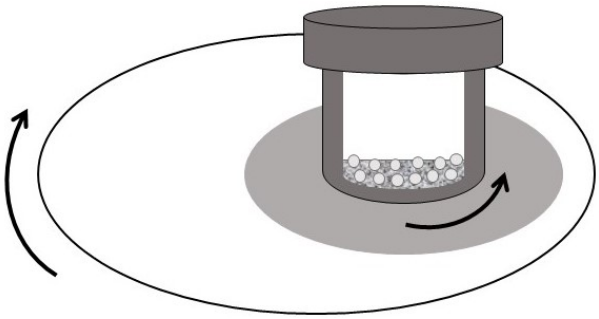

Figure 3.1: Depiction of ball-milling setup.

3.1.3 Hydrogen annealing station

A hydrogen annealing station (Figure 3.2) was used to heat-treat the samples. The material was sealed in a stainless-steel autoclave inside the glove-box. The autoclave was then connected to the gas line and placed in the cylindrical oven. The argon inside the sample holder was evacuated and replaced with approximately 20 bars of hydrogen gas, to prevent decomposition of the sample during heating. The samples were heated at around 160 °C for 72 hours.

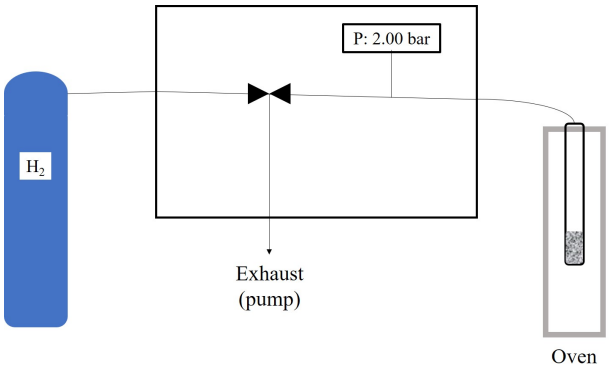

Figure 3.2: Illustration of hydrogen annealing station.

3.2 Characterization

3.2.1 PXD

Initial characterization was performed using a Bruker AXS D8 Advance diffractometer. The machine used a copper anode to supply X-rays of wavelength, $\lambda_{Cu-K_{\alpha 1}}$ = 1.54056 $\mathring{A}$ and $\lambda_{Cu-K_{\alpha 2}}$ = 1.5444 $\mathring{A}$. Capillaries with an inner diameter of 0.5 mm were used for the PXD measurements. The capillaries were filled with approximately 20 mm of powder, inside the glove-box and cut to the correct length ($\sim$ 50 mm) by use of a nail clipper. The open end was then sealed with a drop of super glue and left to dry. The capillaries were mounted and measured for around 15 hours in transmission geometry

often called Debye-Sherrer geometry. The measurements of the *Na-RE-Cl* samples are shown in Figure B.1 in Appendix B.

3.2.2 In-situ SR-PXD

In-situ synchrotron radiation powder X-ray diffraction was conducted for all the samples. The measurements of the iodide samples were performed at ESRF in Grenoble, France, while the chloride samples were measured at Diamond in Didcot, UK.

SNBL BM01 beamline at ESRF

A Dectris Pilatus 2M detector was used for the measurements at BM01. 0.5 mm capillaries were used for the experiments and filled the same way as for the laboratory PXD measurements. A wavelength of $\lambda = 0.6866$ $\AA$ was used and the measurements were taken at 10, 20, 30, 40 and 50 cm, from the goniometer to the detector. The wavelength was determined by measuring a capillary filled with LaB_6 and performing a Rietveld refinement on the pattern. The samples were heated at a constant rate of 5 °C/min from room temperature to 430 °C by a heat blower. The blower was mounted close to the sample and consisted of a fan blowing hot air towards the tip of the capillary. The temperature emitted by the blower and the temperature of the sample will be slightly different, as the air will cool while travelling from the blower to the sample. A temperature calibration was, therefore performed before the measurements were started. The calibration consisted of performing an in-situ measurement on a capillary filled with NaCl. The thermal expansion of NaCl was then used to determine the real temperature of the sample during heating.

Beamline I11 at Diamond

Data was collected in the 2θ range of 2° - 90° using a wide-angle position sensitive detector based on Mythen-2 Si strip modules, with a wavelength of $\lambda = 0.8245$ $\AA$. The samples were heated at a constant rate of 5 °C/min from room temperature to 410 °C by a heat blower. A capillary filled with NaCl was used for both the determination of the wavelength and the calibration of the heat blower.

3.2.3 TGA and DSC

The thermogravimetric analysis (TGA) and differential scanning calorimetry (DSC) measurements were performed simultaneously with a Netzsch STA 449 F3 Jupiter apparatus. Aluminium crucibles with pierced lids, made from the same material were used. The crucible and lid were brought into the glove-box, where about 30 mg of powder was added to the crucible and spread evenly on the bottom. The experiments were conducted with heating rates of 2, 5, 10 and 20 °C/min from room temperature to 400 °C under argon flow.

3.3 PXD analysis

3.3.1 EVA

The XRD software Diffrac.Suite.EVA was used for phase identification of the one-dimensional diffraction patterns [53]. A search of the software's database was conducted for any known compounds with similar diffraction patterns to the experimental data. For this project, the PDF-4+ 2018 database was used [54].

3.3.2 FOX

The phases that were not found in EVA were indexed using FOX [55]. FOX is an open-source program for the ab-initio structure determination from PXD. Unidentified peaks belonging to the same phase were localized and selected. The program then used an algorithm to suggest the crystal systems and lattice parameters that best corresponded with the observed peaks.

3.3.3 GSAS II

GSAS II is a crystallographic data analysis software based on Python [56]. The program can be used to assess the phase composition of a material, by use of Rietveld refinement.

Structural refinements were performed on the room temperature and in-situ SR-PXD data. A Pseudo-Voigt function was used to describe the calculated profiles, while the background was fit to a Chebyshev function. The refinements were conducted by first refining the unit cell parameters of the phases in order to get the correct position of the reflections. The peak profiles were then refined by altering the particle size and strain in the phases. By modifying the temperature factors and atomic positions, the peak intensities were refined. If the sample contained an unknown phase and a probable unit cell was found in FOX, the phase was included by Pawley refinement.

The crystal structures for all the phases except $Na_2RE_2(BH_4)_5I_3$, were retrieved from the Inorganic Crystal Structure Database in the form of Crystal Information Files (CIFs) [57]. The structure for the $Na_2RE_2(BH_4)_5I_3$ phase was modeled by using a CIF for $Na_2La_2(BH_4)_5I_3$, made by one of the researchers at IFE [16]. An overview of the CIFs used for the refinements can be found in Table C.1 in Appendix C.

Chapter 4

Results and discussion

4.1 Iodide samples *Na-RE-I*

This thesis is a continuation of the Fall 2018 Specialization project, *Synthesis and characterization of sodium rare-earth borohydride halides*, where the synthesis and characterization of the as-milled iodide samples were conducted [17]. In this chapter, the thermal properties of the iodide samples are reported and discussed based on in-situ SR-PXD and TGA-DSC measurements.

4.1.1 In-situ SR-PXD

The in-situ SR-PXD measurements showed that the $Na_2RE_2(BH_4)_5I_3$ phases (*RE* = Ce, Pr, Nd, Gd and Tb) decomposed in the temperature range of 274-287 °C. After decomposition peaks from unknown phases appeared in all the samples, except in *Na-Er-I*. This suggests that chemical reactions were activated during heating, resulting in unreported phases. It could also be possible that the crystallization of amorphous phases occurred in this temperature range. The degree of iodide substitution in the solid-solution, $Na(BH_4)_{1-x}I_x$ increased from RT to 360 °C. This was also the case for the samples that contained two solid-solutions, *Na-Gd-I* and *Na-Tb-I*.

RE = Ce, Pr and Nd. The in-situ SR-PXD measurements of *Na-RE-I* (*RE* = Ce, Pr and Nd) are shown in Figures 4.1 - 4.3, where the heat map has been divided into different temperature regions. At room temperature the samples contained $Na_2RE_2(BH_4)_5I_3$ and a solid-solution of NaI and $NaBH_4$. The *Na-Pr-I* and *Na-Nd-I* samples had significant amounts of the starting material, REI_3. Temperature region **1** starts at RT and ends at the decomposition temperature of the $Na_2RE_2(BH_4)_5I_3$ phase. Temperature region **1** starts at RT and ends at the decomposition temperature of the $Na_2RE_2(BH_4)_5I_3$ phase. At the end of the region peaks from unidentified phases appear in all the three samples.

For *Na-Ce-I* two unknown compounds were observed after the decomposition of $Na_2Ce_2(BH_4)_5I_3$ at T = 281 °C (Figure 4.1). Bragg reflections for one of the unidentified compounds increased and then disappeared during heating in temperature region **2** (281-306 °C). The other unknown phase was present in both temperature regions **2** and **3** and also at the end of the measurement, T = 360 °C. Decomposition of $Na_2Pr_2(BH_4)_5I_3$ occurred at T = 287 °C (Figure 4.2). One unidentified phase appeared at the start of temperature region **2** (287-360 °C) and was present throughout the whole region.

After the decomposition of $Na_2Nd_2(BH_4)_5I_3$ at T = 286 °C, two unidentified phases appeared in the diffraction pattern of *Na-Nd-I* (Figure 4.3). Bragg reflections from the first phase emerged at the start of temperature region **2** (286-360 °C), while the peaks from the other appeared at the end of temperature region **2**. Both unknown phases were present at the end of the measurement. The second unknown phase was indexed, and Pawley refinements were conducted to evaluate if the correct structure and unit cell parameters had been chosen. Both indexing and refinement required several attempts to find a good match. The phase that showed the best fit had a body-centered monoclinic structure (space group $I2/m$ with unit cell parameters of a = 9.724 $\AA$, b = 3.634 $\AA$, c = 9.175 $\AA$ and β = 137.88°. However, from the Pawley refinement, it was apparent that the suggested unit cell was not a perfect fit, as there were several peaks it could not account for.

The unidentified peaks at around 2θ = 5° and 19° appeared in all the three samples at T = 280 °C. As the position of these peaks varied in each sample, it is assumed that the unknown phase contains rare-earth atoms and is most likely a decomposition product from $Na_2RE_2(BH_4)_5I_3$. Since only two peaks were observed from this phase, it was not possible to index them and assign a unit cell.

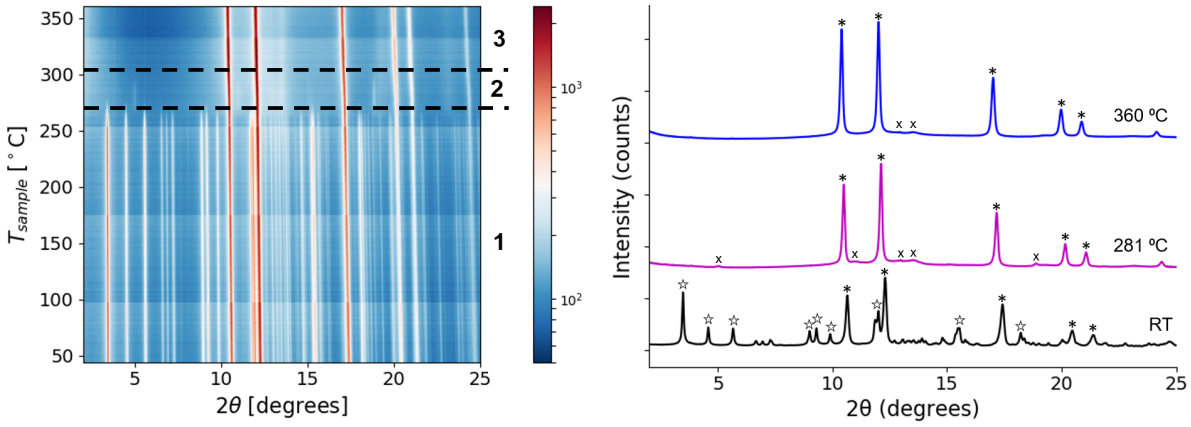

(a) **(b)**

Figure 4.1: (a) In-situ SR-PXD of *Na-Ce-I* measured from RT to T = 360 °C, $\Delta T/\Delta t$ = 5 °C/min (λ = 0.6866 $\AA$). **(b)** SR-PXD at selected temperatures, where NaI ($*$), $Na_2Ce_2(BH_4)_5I_3$ ($\star$), and unidentified peaks ($\times$).

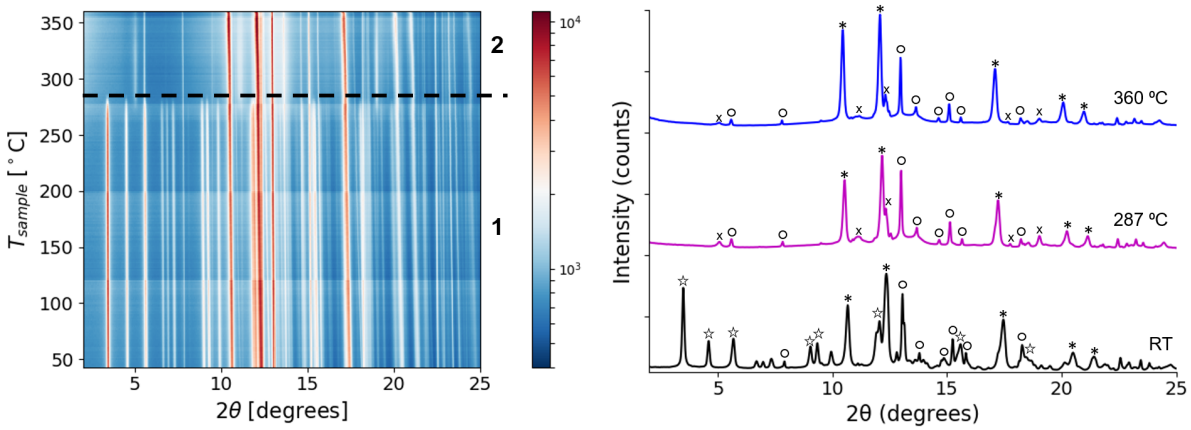

(a) **(b)**

Figure 4.2: (a) In-situ SR-PXD of *Na-Pr-I* measured from RT to T = 360 °C, $\Delta T/\Delta t$ = 5 °C/min (λ = 0.6866 *Å*). **(b)** SR-PXD at selected temperatures, where NaI ($*$), PrI_3 ($\circ$), $Na_2Pr_2(BH_4)_5I_3$ ($\star$), and unidentified peaks ($\times$).

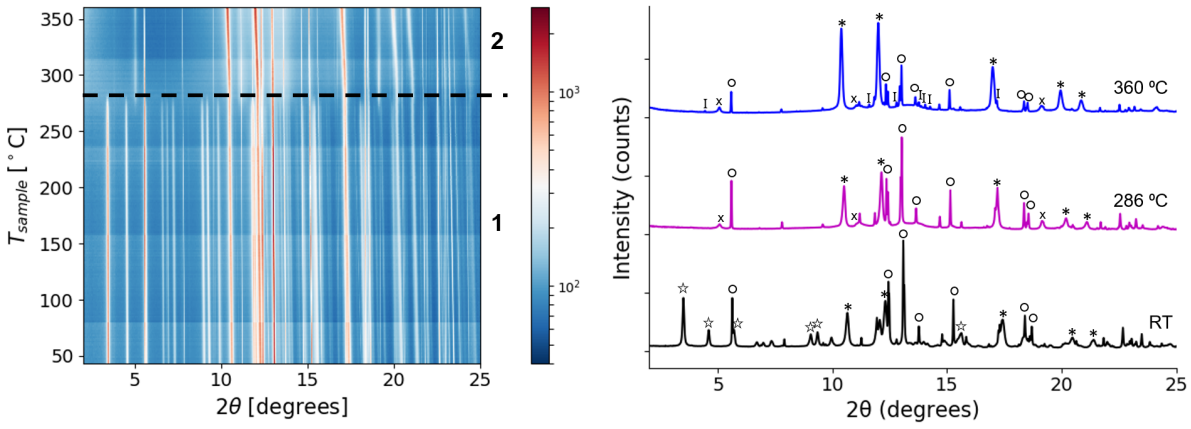

(a) **(b)**

Figure 4.3: (a) In-situ SR-PXD of *Na-Nd-I* measured from RT to T = 360 °C, $\Delta T/\Delta t$ = 5 °C/min (λ = 0.6866 *Å*). **(b)** SR-PXD at selected temperatures, where NaI ($*$), NdI_3 ($\circ$), $Na_2Nd_2(BH_4)_5I_3$ ($\star$), indexed phase (I) and unidentified peaks ($\times$).

RE* = *Gd and Tb. Figures 4.4 and 4.5 present the SR-PXD measurements for *Na-Gd-I* and *Na-Tb-I*. The room temperature diffraction patters showed reflections from $Na_2RE_2(BH_4)_5I_3$, REI_3 and α-$RE(BH_4)_3$ in both samples. The samples also contained two solid-solutions of NaI and $NaBH_4$, where one was NaI rich while the other was $NaBH_4$ rich. *Na-Gd-I* showed additional Bragg reflections belonging to GdOI at RT. At the end of temperature region **1** the decomposition of α-$RE(BH_4)_3$ occurs while at the end of temperature region **2** the $Na_2RE_2(BH_4)_5I_3$ phase decomposes.

α-$Gd(BH_4)_3$ decomposed at the end of temperature region **1** (RT-227 °C) (Figure 4.4). At the start of temperature region **2** peaks belonging to Na_3GdI_6 appeared, in addition to a significant increase in the peak intensity for $Na_2Gd_2(BH_4)_5I_3$. Simultaneously a drop in intensity for GdI_3 and $NaBH_4$ occurred, suggesting that GdI_3 and $NaBH_4$ reacted to form Na_3GdI_6 and some amorphous product. Decomposition of $Na_2Gd_2(BH_4)_5I_3$ took place at the end of temperature region **2** (227-274 °C). A set of unidentified peaks appeared at the start of temperature region **3**. At the end of temperature region **3** (274-360 °C) there was a notable decrease in the peak intensity for GdI_3, together with an increase in intensity for Na_3GdI_6 and NaI.

The decomposition route of *Na-Tb-I* was very similar to that of *Na-Gd-I* (Figure 4.5). At the end of temperature region **1** (RT-237 °C) α-$Tb(BH_4)_3$ decomposed and peaks from Na_3TbI_6 appeared. Around the same temperature there was also a noticeable increase in the peak intensity for $Na_2Tb_2(BH_4)_5I_3$ and decrease in intensity for TbI_3 and $NaBH_4$. Na_3TbI_6 is assumed to be formed by the same reaction as suggested for Na_3GdI_6. Decomposition of $Na_2Tb_2(BH_4)_5I_3$ occurred at the end of temperature region **2** (237-282 °C) and two unidentified peaks appeared. At the end of temperature region **3** (282-360 °C) the peak intensity for TbI_3 decreased while there was an increase in intensity for Na_3TbI_6 and NaI. Both samples contained two unidentified peaks at around $2\theta = 5°$ and 19°. It is assumed that the unidentified peaks belong to the same unknown phase found in *Na-RE-I* (*RE* = Ce, Pr and Nd).

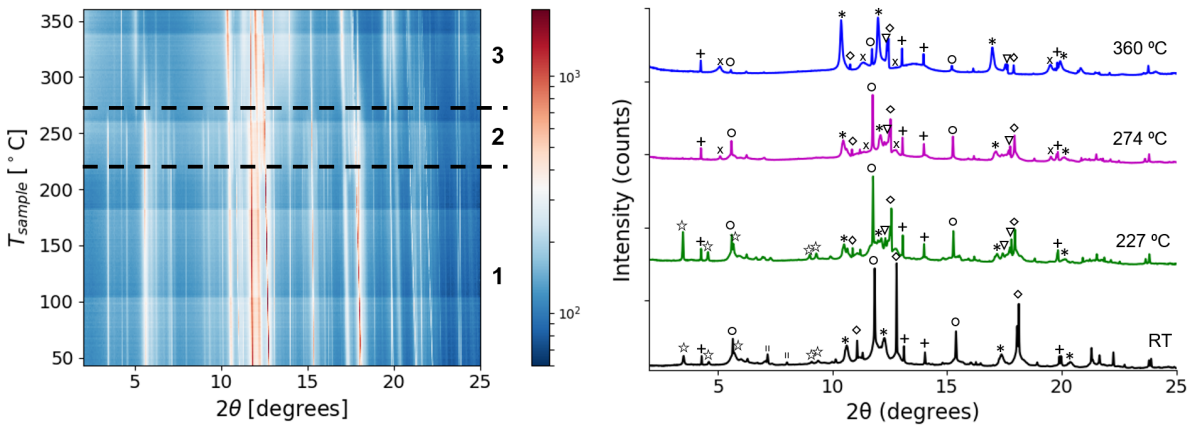

(a) **(b)**

Figure 4.4: (a) In-situ SR-PXD of *Na-Gd-I* measured from RT to T = 360 °C, $\Delta T/\Delta t$ = 5 °C/min (λ = 0.6866 *Å*). **(b)** SR-PXD at selected temperatures, where NaI ($*$), GdI_3 ($\circ$), $Na_2Gd_2(BH_4)_5I_3$ ($\star$), $NaBH_4$ ($\diamond$), α-$Gd(BH_4)_3$ ($\|$), GdOI ($+$), Na_3GdI_6 ($\triangledown$) and unidentified peaks ($\times$).

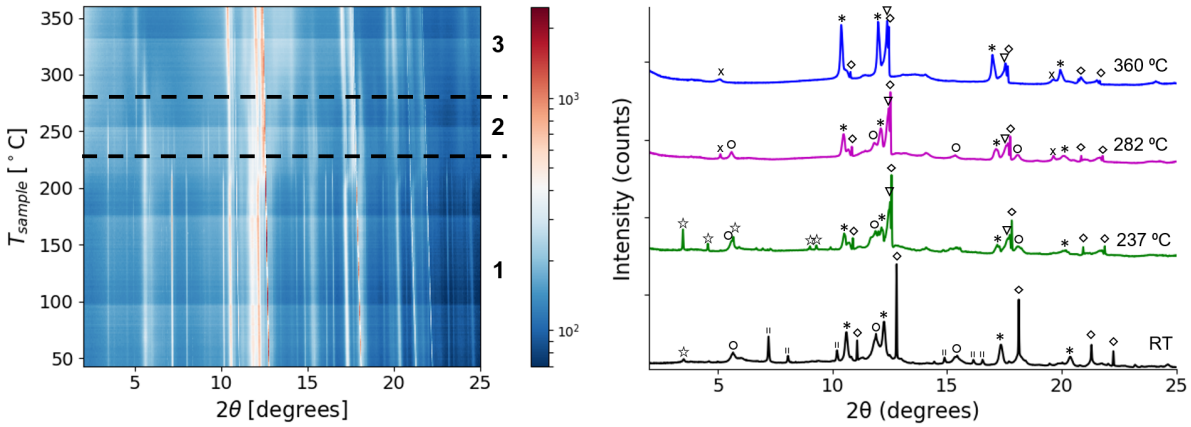

(a) **(b)**

Figure 4.5: **(a)** In-situ SR-PXD of *Na-Tb-I* measured from RT to T = 360 °C, $\Delta T/\Delta t$ = 5 °C/min (λ = 0.6866 $\AA$). **(b)** SR-PXD at selected temperatures, where NaI ($*$), TbI_3 ($\circ$), $Na_2Tb_2(BH_4)_5I_3$ ($\star$), $NaBH_4$ ($\diamond$), α-$Tb(BH_4)_3$ ($\|$), Na_3TbI_6 ($\triangledown$) and unidentified peaks ($\times$).

RE* = *Y and Er. The in-situ SR-PXD measurements of *Na-Y-I* and *Na-Er-I* are presented in Figures 4.6 and 4.7. At room temperature the samples consisted of α-*RE*$(BH_4)_3$ and $Na(BH_4)_{1-x}I_x$, while in *Na-Er-I* additional Bragg reflections belonging to ErOI were identified. The line between temperature region **1** and **2** marks the decomposition of the α-*RE*$(BH_4)_3$ phase.

The Bragg reflections for α-$Y(BH_4)_3$ disappeared at T = 240 °C and reflections from an unknown compound emerged at the end of temperature region **1** (RT-240 °C) (Figure 4.6). The unknown phase was indexed, where several attempts were needed to find a phase that showed a good fit in the Pawley refinements. The phase with the best fit had a primitive monoclinic structure (space group $P2/m$) with lattice parameters of a = 3.477 $\AA$, b = 4.007 $\AA$, c = 7.810 $\AA$ and β = 99.09°. The unknown phase decomposed at the end of temperature region **2** (240-300 °C). As the unidentified phase showed peaks at 2θ = 5° and 20° it is possible that this phase is the same as found in all the other samples. This could suggest that it is not the decomposition of $Na_2RE_2(BH_4)_5I_3$ that promotes the production of the unknown phase, but rather that the phase is amorphous at RT and crystallizes during heating. On the other hand, the unknown compound in *Na-Y-I* contained peaks that were not found in the other samples, indicating that it could be a different phase. Upon heating the α-$Er(BH_4)_3$ phase decomposed at T = 215 °C without formation of any new crystalline compounds (Figure 4.7).

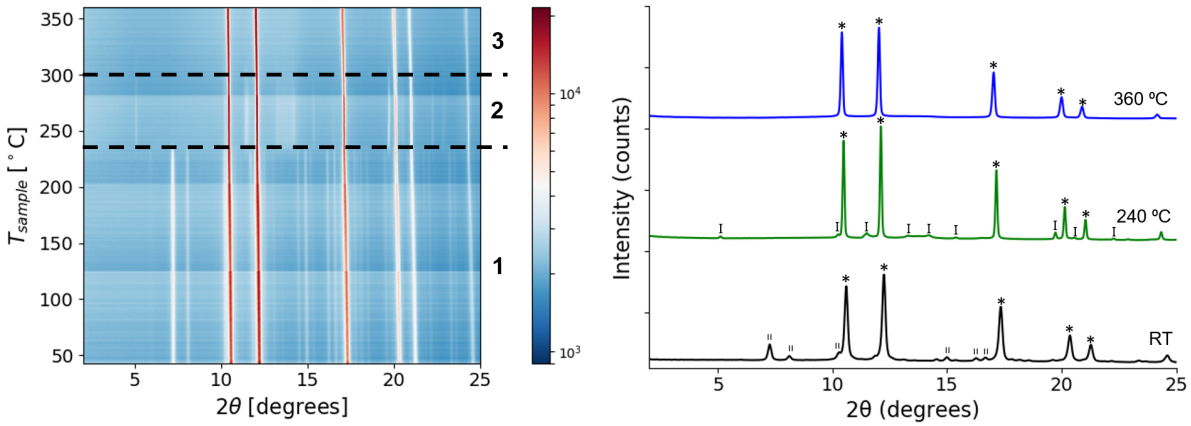

(a) **(b)**

Figure 4.6: **(a)** In-situ SR-PXD of *Na-Y-I* measured from RT to T = 360 °C, $\Delta T/\Delta t$ = 5 °C/min (λ = 0.6866 *Å*). **(b)** SR-PXD at selected temperatures, where NaI ($*$), α-$Y(BH_4)_3$ ($\|$) and indexed phase (I).

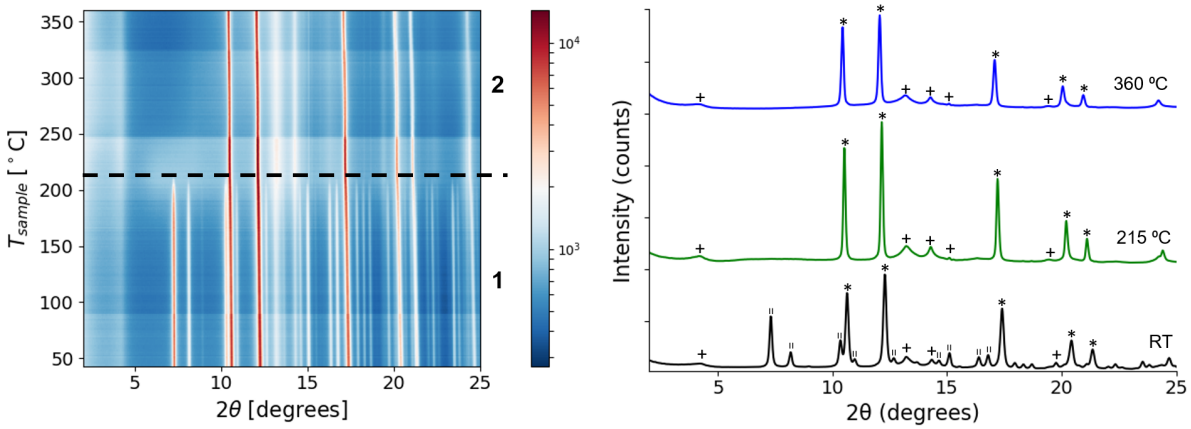

(a) **(b)**

Figure 4.7: **(a)** In-situ SR-PXD of *Na-Er-I* measured from RT to T = 360 °C, $\Delta T/\Delta t$ = 5 °C/min (λ = 0.6866 *Å*). **(b)** SR-PXD at selected temperatures, where NaI ($*$), α-$Er(BH_4)_3$ ($\|$) and ErOI ($+$).

4.1.2 TGA, DSC and Kissinger analyses

Common characteristics of the TGA and DSC measurements were observed in a manner similar to the SR-PXD measurements. The strongest peak in each DSC measurement had a broad tail on the right-hand side of the peak, making it difficult to determine the number of peaks present. All the samples showed minor mass losses occurring between 300 to 400 °C, indicating the release of small amounts of a volatile material. The decomposition temperatures of both the $Na_2RE_2(BH_4)_5I_3$ and α-$RE(BH_4)_3$ phases were observed to be somewhat lower by TGA and DSC than by in-situ SR-PXD. This was, however, expected as the build-up of hydrogen gas in the capillary creates a back pressure that suppresses the decomposition of the phases. The back pressure during the TGA-DSC measurements is much lower due to the pierced lid.

RE = Ce, Pr and Nd. Figure 4.8 presents the TGA-DSC measurements of the as-milled samples from RT to 400 °C with a heating rate of 5 °C/min. The DSC data for *Na-Ce-I* showed one large endothermic peak with a smaller peak on its right shoulder at T = 260-280 °C. The two events may be due to the decomposition of $Na_2Ce_2(BH_4)_5I_3$. However, from the in-situ SR-PXD data, it seemed as though the Bragg reflections of $Na_2Ce_2(BH_4)_5I_3$ disappeared simultaneously and not gradually as they would have done in a two-step decomposition. It is, therefore, possible that the first endothermic peak is affiliated with the decomposition of $Na_2Ce_2(BH_4)_5I_3$, while the second is due to the decomposition of an amorphous phase, or the opposite. A total weight loss of 1.92 wt% occurred during these two events. The $Na_2Ce_2(BH_4)_5I_3$ phase had a weight fraction, W_f = 0.480 at RT in the sample. The release of hydrogen during decomposition of $Na_2Ce_2(BH_4)_5I_3$ accounts for a weight loss of 1.24 wt%. The remaining weight loss can be due to hydrogen release from $Na(BH_4)_{1-x}I_x$ as a result of increased iodide substitution, decomposition of an amorphous phase or the release of diborane B_2H_6 or higher boranes.

The *Na-Pr-I* and *Na-Nd-I* samples both showed single endothermic peaks in the DSC measurements, with peak temperatures of T = 263 °C and T = 265 °C respectively. The total weight loss of *Na-Pr-I* was 1.62 wt%, while *Na-Nd-I* had a total weight loss of 1.39 wt%. The majority of the weight loss is assumed to be the decomposition of the $Na_2RE_2(BH_4)_5I_3$ phases. Hydrogen in $Na_2Pr_2(BH_4)_5I_3$ (W_f = 0.414 at RT) accounts for a weight loss of 1.16 wt% in the *Na-Pr-I* sample, while release of hydrogen during decomposition of $Na_2Nd_2(BH_4)_5I_3$ (W_f = 0.360 at RT) accounts for a weight loss of 1.39 wt%. The remaining weight loss may be due to the same factors as described for *Na-Ce-I*.

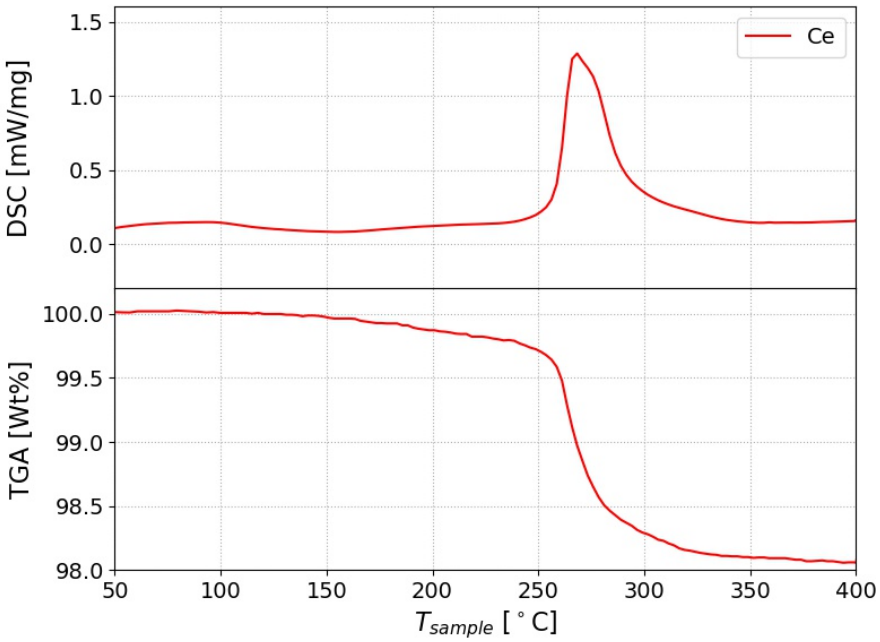

(a) TGA-DSC measurement for *Na-Ce-I*.

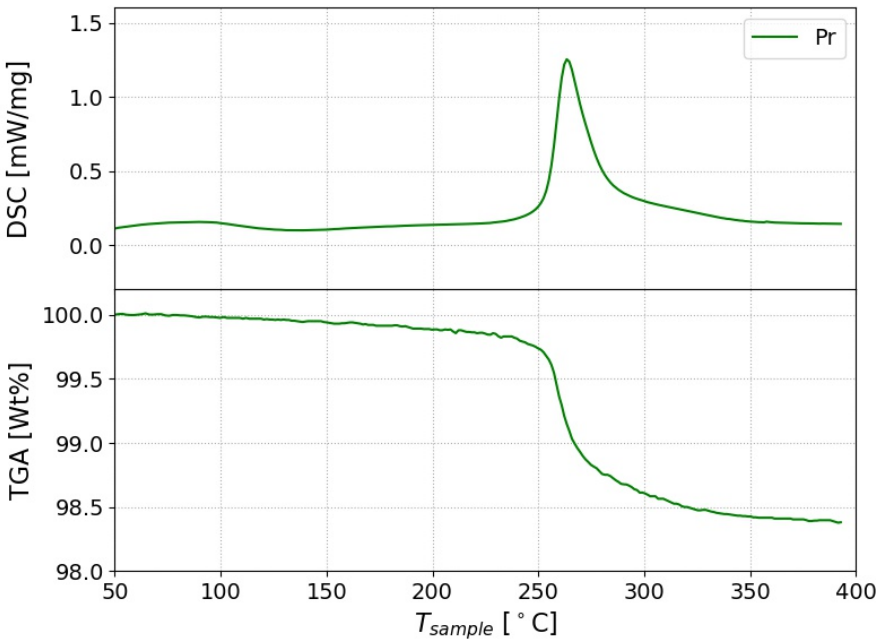

(b) TGA-DSC measurement for *Na-Pr-I*.

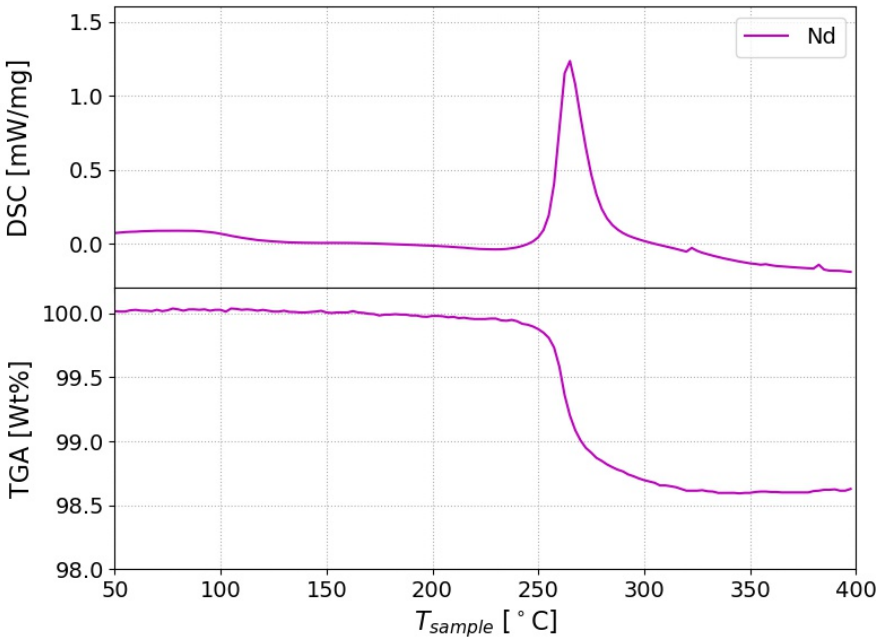

(c) TGA-DSC measurement for *Na-Nd-I*.

Figure 4.8: Results from simultaneous TGA and DSC measured from RT to T = 400 °C, $\Delta T/\Delta t$ = 5 °C/min for *Na-RE-I* (*RE* = Ce, Pr and Nd).

RE = Gd and Tb. The TGA-DSC measurements of the as-milled samples from RT to 400 °C with a heating rate of 5 °C/min are shown in Figure 4.9. The DSC measurement of *Na-Gd-I* showed a small endothermic peak at T = 227 °C and a larger peak at T = 269 °C. The first peak is assumed to be the decomposition of α-$Gd(BH_4)_3$, while the second is the decomposition of $Na_2Gd_2(BH_4)_5I_3$. The reported decomposition temperature of a phase pure α-$Gd(BH_4)_3$ sample is T = 274 °C [30]. As discussed in the literature review, a deviation from the reported value can be due to by-products reacting with the *RE* borohydride or promoting early decomposition by acting as catalysts, consequently lowering the decomposition temperature of the *RE* borohydride phase. At room temperature, *Na-Gd-I* contained six phases, and it is therefore not surprising that the decomposition temperature of α-$Gd(BH_4)_3$ in the sample was lower than the reported value. The two events in *Na-Gd-I* result in a total weight loss of 1.07 wt%. The hydrogen in α-$Gd(BH_4)_3$ (W_f = 0.009 at RT) and $Na_2Gd_2(BH_4)_5I_3$ (W_f = 0.109 at RT) accounts for weight losses of 0.05 wt% and 0.27 wt% respectively, in the sample.

Na-Tb-I has three DSC peaks, one small peak at T = 215 °C, another at T = 250 °C and a third at T = 266 °C. The first two peaks are assumed to be the two-step decomposition of α-$Tb(BH_4)_3$, which fits very well with reported values, T = 213 °C and T = 253 °C [29]. The last peak is presumed to be the decomposition of $Na_2Tb_2(BH_4)_5I_3$. The total mass loss in the sample was 1.18 wt%. The hydrogen in α-$Tb(BH_4)_3$ (W_f = 0.035 at RT) and $Na_2Tb_2(BH_4)_5I_3$ (W_f = 0.025 at RT) accounts for weight losses of 0.21 wt% and 0.06 wt% respectively, in the sample. In both *Na-Gd-I* and *Na-Tb-I* it is assumed that the excess weight loss is due to hydrogen release from $Na(BH_4)_{1-x}I_x$ as a result of increased iodide substitution, decomposition of an amorphous phase or the release of diborane B_2H_6 or higher boranes.

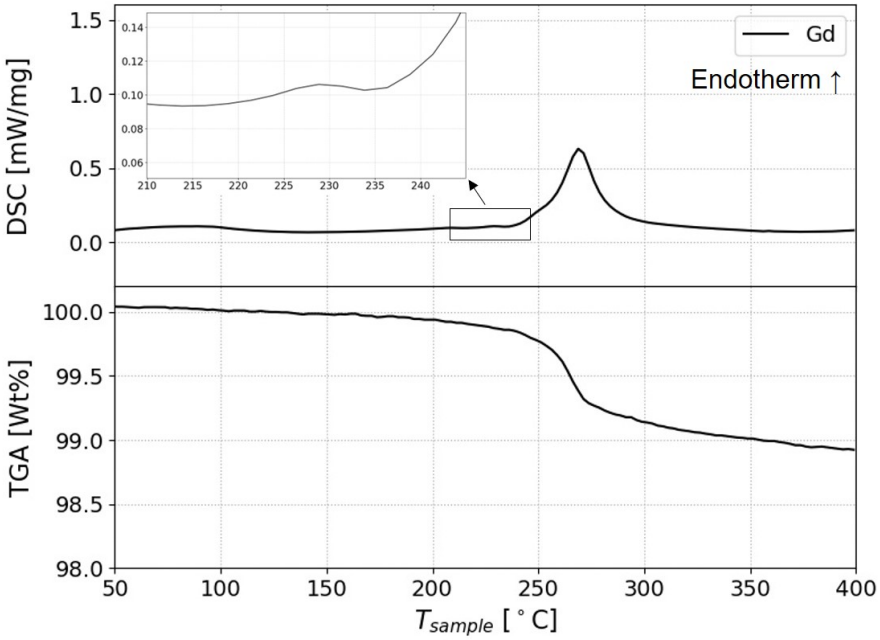

(a) TGA-DSC measurement for *Na-Gd-I*.

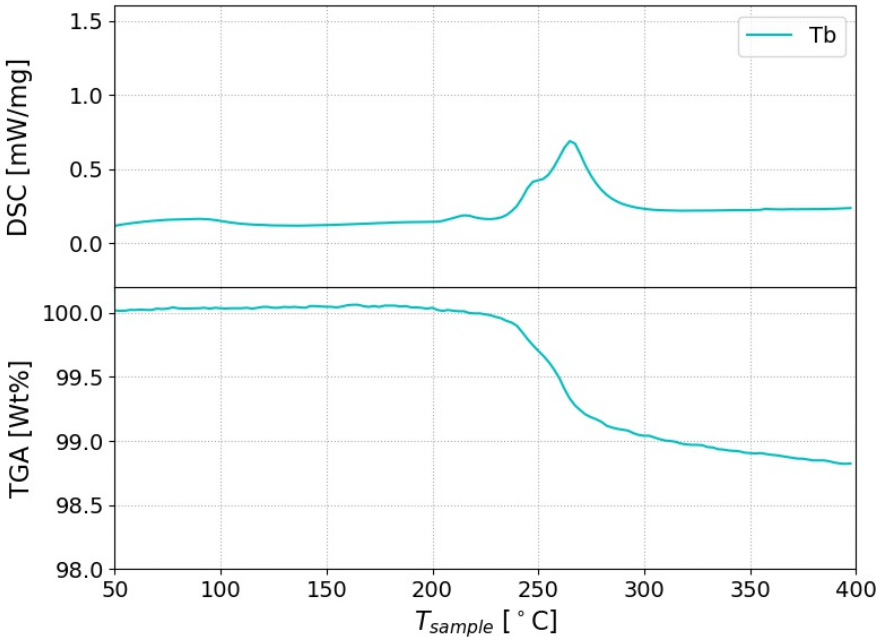

(b) TGA-DSC measurement for *Na-Tb-I*.

Figure 4.9: Results from simultaneous TGA and DSC measured from RT to $T = 400$ °C, $\Delta T/\Delta t = 5$ °C/min for *Na-RE-I* (*RE* = Gd and Tb).

RE = Y and Er. Figure 4.10 shows the TGA-DSC measurements of the as-milled samples from RT to 400 °C with a heating rate of 5 °C/min. Two large endothermic peaks were present in the DSC measurement of *Na-Y-I* and are assumed to be a two-step decomposition of α-$Y(BH_4)_3$, with peak temperatures at T = 244 °C and T = 263 °C. The mass loss occurred in two abrupt steps with an overall weight loss of 1.90 wt%. The observed mass loss is almost equal to the calculated hydrogen content of the α-$Y(BH_4)_3$ phase 1.88 wt%, where the weight fraction of α-$Y(BH_4)_3$ in the ample was 0.207 at RT.

The *Na-Er-I* sample had a small, broad endothermic DSC peak at T = 261 °C, which is assumed to be the decomposition of α-$Er(BH_4)_3$. The reported decomposition temperature of a phase pure α-$Er(BH_4)_3$ sample is T = 277 °C [46]. *Na-Er-I* was a multi-phase sample consisting of three phases at room temperature. It is, therefore, possible that the decomposition temperature of α-$Er(BH_4)_3$ was affected by the presence of the other phases. As the peak was so broad, it was difficult to determine if the signal was one broad peak or multiple narrower peaks. The overall weight loss of the sample was 0.99 wt%. The α-$Er(BH_4)_3$ phase (W_f = 0.163 at RT) had a hydrogen content of 0.93 wt% in the sample, which is quite close to the samples mass loss.

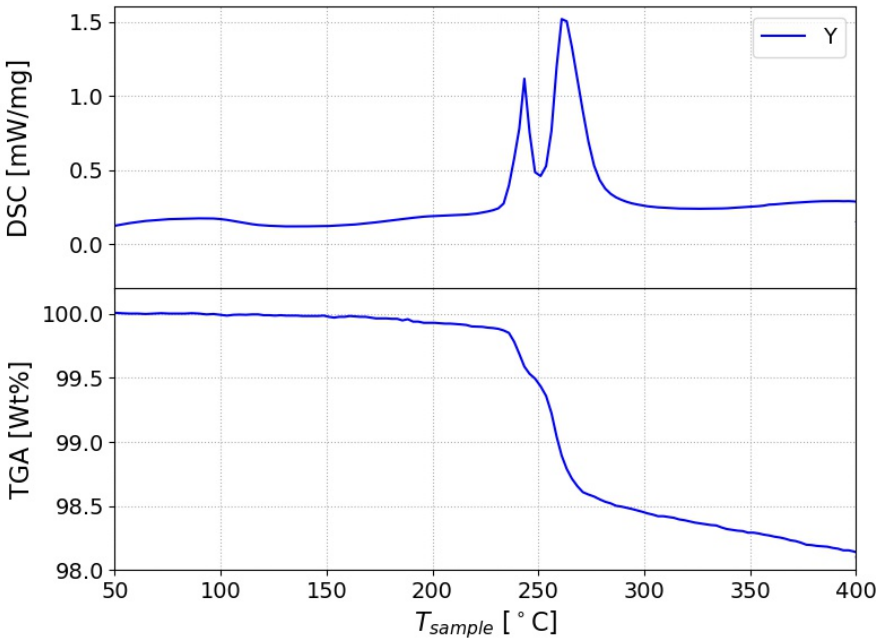

(a) TGA-DSC measurement for *Na-Y-I*.

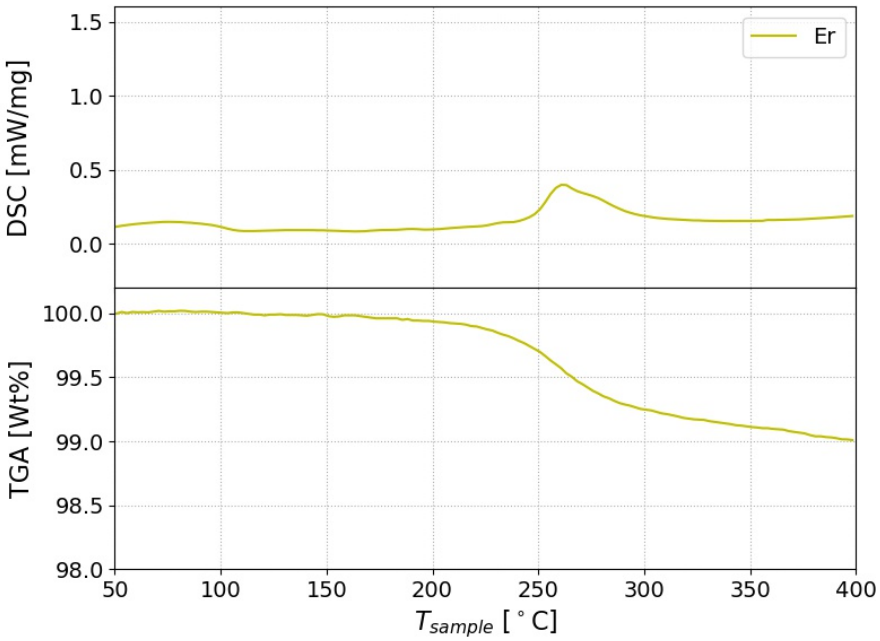

(b) TGA-DSC measurement for *Na-Er-I*.

Figure 4.10: Results from simultaneous TGA and DSC measured from RT to $T = 400$ °C, $\Delta T/\Delta t = 5$ °C/min for *Na-RE-I* (*RE* = Y and Er).

An inverse correlation between the decomposition temperature of the metal borohydrides and the Pauling electronegativity of the metal cation has been well-established. The increasing cation electronegativity results in a greater pull on the electrons in the BH_4^- units, thus destabilizing the B-H bond. The onset temperature, T_{onset} from the DSC peaks for the decomposition of $Na_2RE_2(BH_4)_5I_3$ have been plotted against the Pauling electronegativities, χ_P of the rare-earth cations (Figure 4.11a). For *Na-Ce-I* where it was uncertain if $Na_2Ce_2(BH_4)_5I_3$ decomposed in one or two steps, the onset temperature of the largest peak has been plotted. From Figure 4.11a there seems to be no systematic change in the onset temperature when the cation electronegativity increases. This is surprising as the data does not follow the reported trend. It is important to note that the range in the electronegativity for the *RE* cations is narrow (1.10 to 1.27), and therefore the decomposition temperatures are expected to only have small variations.

A Kissinger analysis was conducted for the decomposition of $Na_2RE_2(BH_4)_5I_3$ (Figure 4.12). For *Na-Ce-I* the peak temperature of the largest peak was used for the analysis. From the analysis, the activation energies for each decomposition were found and have been plotted against the electronegativity of the rare-earth cations in Figure 4.11b. The figure shows a positive and almost linear trend, suggesting that as the electronegativity of the cation increases the more energy is required to activate the decomposition of $Na_2RE_2(BH_4)_5I_3$. The decomposition temperature of a phase is determined by the kinetics and thermodynamics of the decomposition reaction. A decomposition reaction with a high activation energy will exhibit slow kinetics. As all the $Na_2RE_2(BH_4)_5I_3$ phases had around the same onset temperature, the $Na_2Gd_2(BH_4)_5I_3$ and $Na_2Tb_2(BH_4)_5I_3$ phases are assumed to be the least thermodynamic stable phases as they have the highest activation energies. It, therefore, seems as though the thermodynamic stability of the $Na_2RE_2(BH_4)_5I_3$ phases decreases with increasing electronegativity of the rare-earth cation.

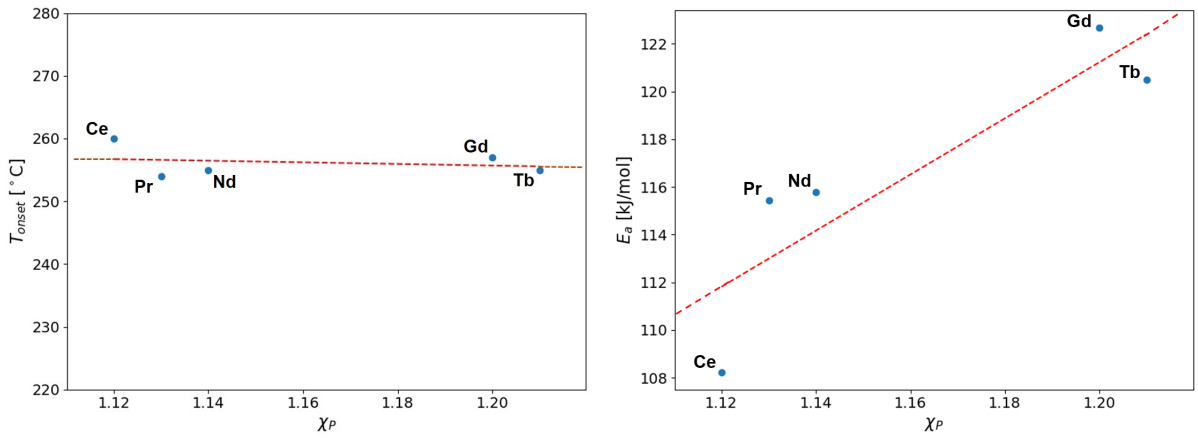

(a) **(b)**

Figure 4.11: Plots showing the correlation between **(a)** onset temperature and **(b)** activation energy for the decomposition of $Na_2RE_2(BH_4)_5I_3$ (RE = Ce, Pr, Nd, Gd and Tb). The onset temperatures are taken from the DSC measurements where $\Delta T/\Delta t = 5$ °C/min.

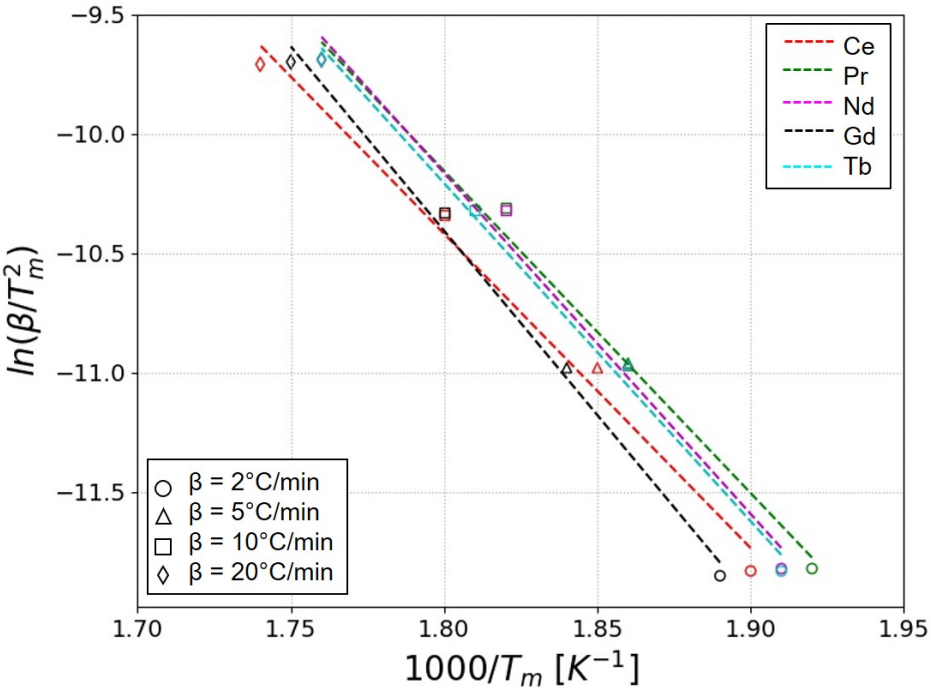

Figure 4.12: Kissinger analysis for the decomposition of $Na_2RE_2(BH_4)_5I_3$ (RE = Ce, Pr, Nd, Gd and Tb).

4.2 Chloride samples *Na-RE-Cl*

4.2.1 Extent of reaction and phase composition

SR-PXD data collected at room temperature was used for phase identification. The diffraction patterns were imported to the EVA software, where the background was subtracted, and a search for all known crystalline phases consisting of the relevant elements was carried out. The SR-PXD patterns of the samples, *Na-RE-Cl* (*RE* = Ce, Tb and Yb) are shown in Figure 4.13, where the most intense Bragg reflections for each phase are identified and marked in the figure. A qualitative analysis based on the diffraction data is summarized in Table 4.1.

From Figure 4.13 it is apparent that the *Na-RE-Cl* samples behave differently from the *Na-RE-I* samples. There are no indications that a $Na_2RE_2(BH_4)_5Cl_3$ phase has been formed in any of the samples, instead significant amounts of $NaRE(BH_4)_2Cl_2$ and Na_3RECl_6 were present in *Na-Tb-Cl* and *Na-Yb-Cl*. It is therefore proposed that the two samples follow the reactions given in Equation 4.1-4.3. This reaction path was proposed by *Ravnsbæk* when the $NaY(BH_4)_2Cl_2$ phase was first reported, where it is suggested that reaction 4.2 and 4.3 are competing reactions [45]. However as both samples contained peaks from unknown phases, it is possible that other competing reactions are also taking place. The *Na-Ce-Cl* sample only contained $CeCl_3$ and a solid-solution of $NaBH_4$ and NaCl at room temperature. All the samples contained considerable amounts of the starting materials ($RECl_3$ and $NaBH_4$), indicating that the reactions were not completed. This can be due to many factors such as unsuitable milling conditions.

$$2NaBH_4 + RECl_3 \rightarrow NaRE(BH_4)_2Cl_2 + NaCl \tag{4.1}$$

$$3NaCl + RECl_3 \rightarrow Na_3RECl_4 \tag{4.2}$$

$$(1-x)NaBH_4 + xNaCl \rightarrow Na(BH_4)_{1-x}Cl_x \tag{4.3}$$

Table 4.1: Overview of qualitative amounts, X (trace), XX (moderate amount) and XXX (main phase), of each phases observed in the *Na-RE-Cl* samples at RT.

	Na-Yb-Cl	*Na-Tb-Cl*	*Na-Ce-Cl*
$RECl_3$	XX	XXX	XXX
$NaBH_4$	XX	XX	
$Na(BH_4)_{1-x}Cl_x$			XXX
$NaRE(BH_4)_2Cl_2$	XXX	XXX	
Na_3RECl_6	X	X	
Unidentified phase	X	X	

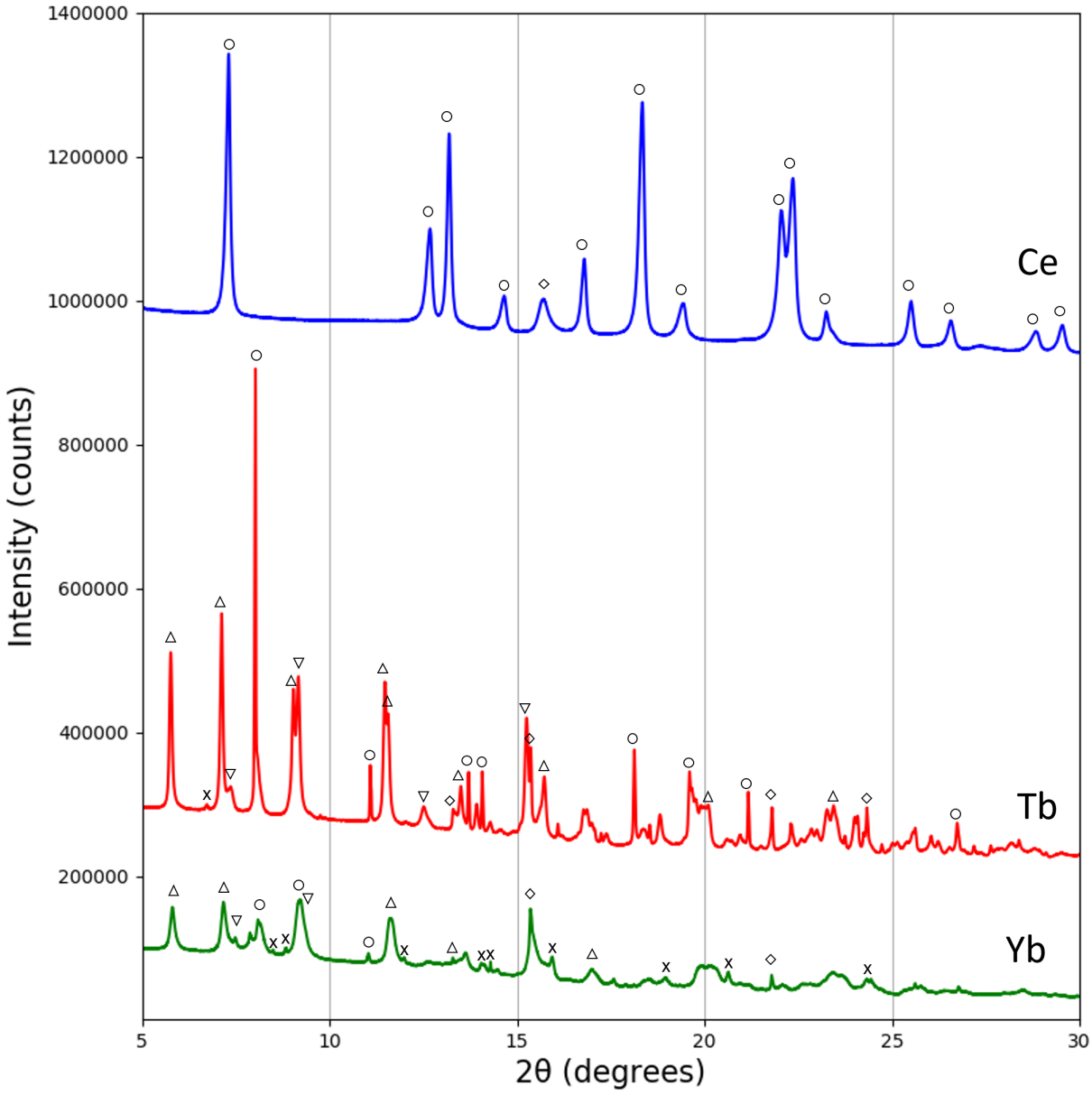

Figure 4.13: Figure showing phases present in each sample at RT. $NaBH_4$ ($\diamond$), $RECl_3$ ($\circ$), $NaRE(BH_4)_2Cl_2$ ($\triangle$), Na_3RECl_6 ($\triangledown$) and unidentified peaks ($\times$).

3 $NaBH_4$ + $YbCl_3$. At room temperature the sample consisted of $NaYb(BH_4)_2Cl_2$, Na_3YbCl_6, $YbCl_3$ and a small amount of $NaBH_4$. An unidentified phase was also observed, corresponding to multiple small reflections. Several attempts were made to perform a structural refinement of the sample with different plausible phases, to identify the phase. However a suitable phase was not found. The refinement of *Na-Yb-Cl* at RT is shown in Figure 4.14, where $NaYb(BH_4)_2Cl_2$, Na_3YbCl_6, $YbCl_3$ and $NaBH_4$ were included. The weighted *R*-factor of the refinement was 3.451, indicating a good match with the measured data. Table 4.2 presents the weight fractions of the phases.

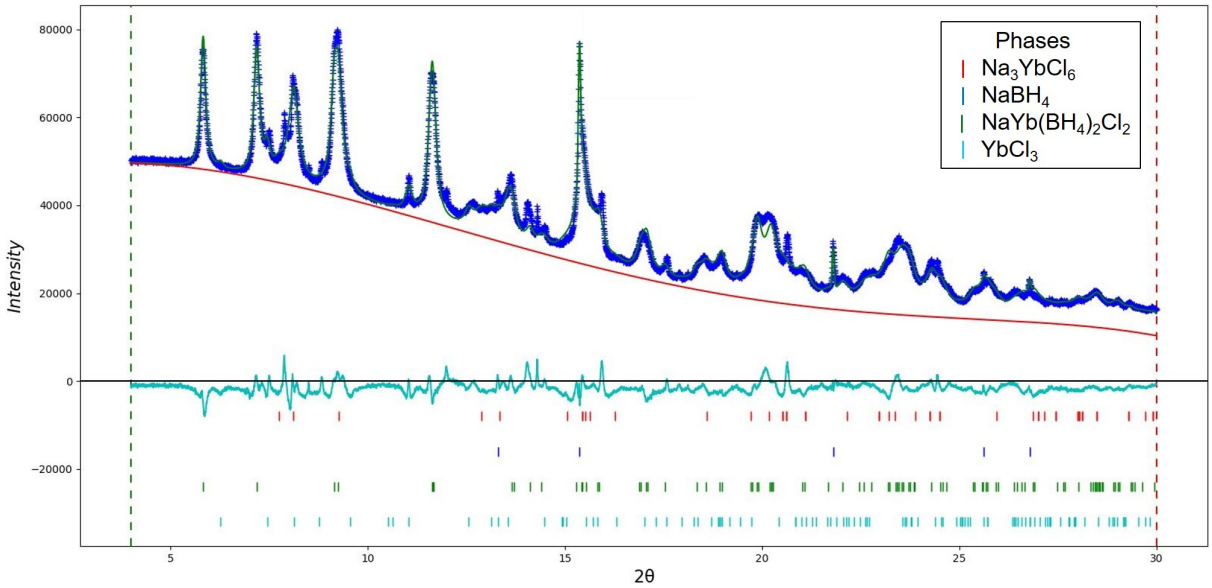

Figure 4.14: Rietveld refinement of *Na-Yb-Cl* from SR-PXD data collected at RT. The blue crosses in the diffraction patterns indicate the observed data (Y^{obs}), while the green line is the calculated profile (Y^{calc}). The red line is the fitted background ($Y^{background}$) and the turquoise line is the difference in intensity between the observed data and the fitted profile ($Y^{obs} - Y^{calc}$).

Table 4.2: The weight and mole fractions of the phases present in *Na-Yb-Cl*.

Phase	Weight fraction [∅]	Mole fraction [∅]
$NaYb(BH_4)_2Cl_2$	0.294	0.105
Na_3YbCl_6	0.276	0.064
$YbCl_3$	0.155	0.059
$NaBH_4$	0.275	0.772

As no solid-solution of $NaBH_4$ and NaCl was formed it is assumed that the sample followed Reactions 4.1 and 4.2. There were no traces of NaCl in the sample, indicating that all NaCl produced in Reaction 4.1 was consumed in Reaction 4.2. This means that in theory the sample should have a 3:1 molar ratio between $NaYb(BH_4)_2Cl_2$ and Na_3YbCl_6. However, this is not the case as the molar ratio was determined to be approximately 1.6:1. This strengthens the theory that other competing reactions are taking place, producing non-crystalline phases. By adding up the number of moles for Na, BH_4, Yb and Cl separately. the molar ratio between them was determined. As the ratio between Na and Yb was not 3:1 but rather 4.7:1 it is assumed that some Yb is

present in an amorphous phase. A 1:3.4 ratio was found for Yb and Cl which is another indication that there is a non-crystalline phase containing Yb in the sample. The ratio between Na and BH_4 was 1.1:1, suggesting that small amounts of BH_4 is also present in an amorphous phase.

3 NaBH₄ + TbCl₃. The diffraction pattern for *Na-Tb-Cl* at RT had strong resemblance to the *Na-Yb-Cl* pattern, with the exception of the large difference in crystallinity between the two samples, especially for the $RECl_3$. Peaks for $NaTb(BH_4)_2Cl_2$, Na_3TbCl_6, $TbCl_3$ and $NaBH_4$ were identified. The sample also contained one Bragg reflection from an unidentified phase. It is assumed that the remaining reflections of this minor phase lies beneath the peaks of the main phases. Figure 4.15 shows the refinement of *Na-Tb-Cl* at RT, where $NaTb(BH_4)_2Cl_2$, Na_3TbCl_6, $TbCl_3$ and $NaBH_4$ were included. The refinement showed a good fit with the measured data with a weighted *R*-factor of 7.782. Table 4.2 presents the weight fractions of the phases.

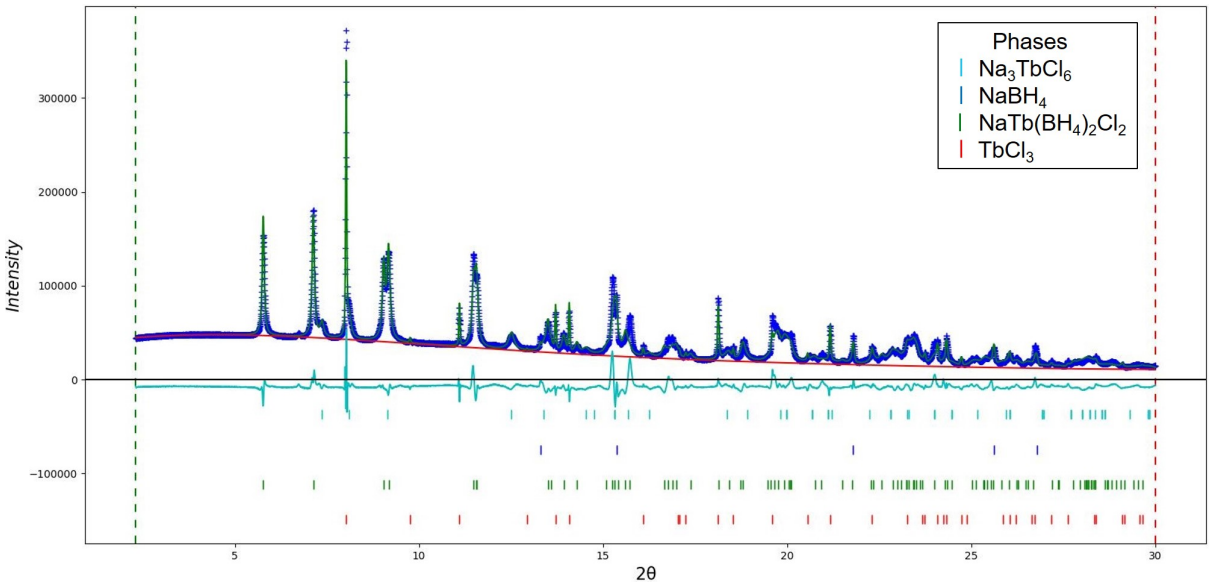

Figure 4.15: Rietveld refinement of *Na-Tb-Cl* from SR-PXD data collected at RT. The blue crosses in the diffraction patterns indicate the observed data (Y^{obs}), while the green line is the calculated profile (Y^{calc}). The red line is the fitted background ($Y^{background}$) and the turquoise line is the difference in intensity between the observed data and the fitted profile ($Y^{obs} - Y^{calc}$).

Table 4.3: The weight and mole fractions of the phases present in *Na-Tb-Cl*.

Phase	Weight fraction [∅]	Mole fraction [∅]
$NaTb(BH_4)_2Cl_2$	0.512	0.454
Na_3TbCl_6	0.301	0.171
$TbCl_3$	0.152	0.143
$NaBH_4$	0.035	0.232

Na-Tb-Cl followed Reactions 4.1 and 4.2 as no solid-solution of $NaBH_4$ and NaCl was present. Like *Na-Yb-Cl* all NaCl produced in Reaction 4.1 was consumed in Reaction 4.2. The molar ratio between $NaTb(BH_4)_2Cl_2$ and Na_3TbCl_6 should therefore be 3:1. The experimental data gave a molar ratio of 2.7:1 between the two phases, which is quite close to the theoretical value. The small deviation may be due to the presence of a competing reaction, producing amorphous phases. The molar ratios of Na, BH_4, Tb and Cl in the sample were determined. A 1.6:1 ratio was found for Na and Tb indicating that significant amounts of Na is incorporated in a non-crystalline phase. The molar ratio of Tb and Cl was approximately 1:3, while the ratio of Na and BH_4 was 1.1:1. This suggests that small amounts of BH_4 is also present in an amorphous phase.

5 $NaBH_4$ + 3 $CeCl_3$. At RT the sample contained Bragg reflections for $CeCl_3$ and $Na(BH_4)_{1-x}Cl_x$. The composition of the solid-solution was determined to be $Na(BH_4)_{0.74}Cl_{0.36}$ from Vegard's law. Figure 4.15 shows the refinement of *Na-Ce-Cl* at RT, where $CeCl_3$ and $NaBH_4$ were refined phases. The refinement had a weighted *R*-factor of 5.025. Table 4.4 presents the weight fractions of the phases.

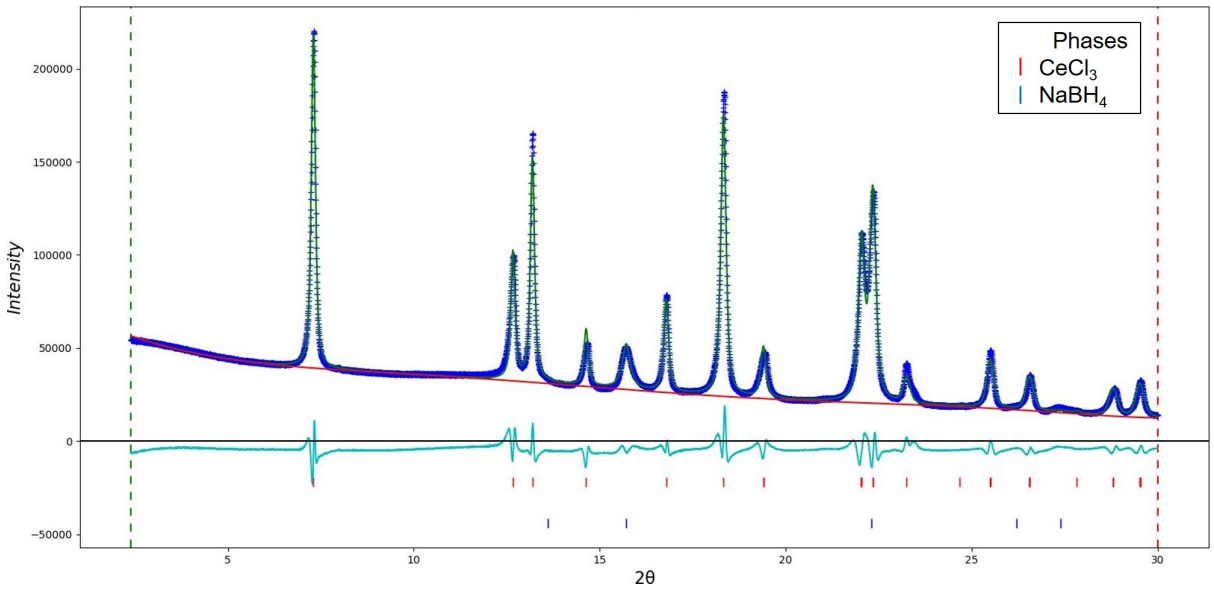

Figure 4.16: Rietveld refinement of *Na-Ce-Cl* from SR-PXD data collected at RT. The blue crosses in the diffraction patterns indicate the observed data (Y^{obs}), while the green line is the calculated profile (Y^{calc}). The red line is the fitted background ($Y^{background}$) and the turquoise line is the difference in intensity between the observed data and the fitted profile ($Y^{obs} - Y^{calc}$).

Table 4.4: The weight and mole fractions of the phases present in *Na-Ce-Cl*.

Phase	Weight fraction [∅]	Mole fraction [∅]
$CeCl_3$	0.488	0.160
$NaBH_4$	0.512	0.840

The molar ratios of Na, BH_4, Ce and Cl were very different from the 5:3 ratio of the reactants, $NaBH_4$ and $CeCl_3$. A 15.7:3 ratio of Na andCe suggests that large amounts of Ce is included in an amorphous phase. The molar ratio of Ce and Cl was 1:4.9 which is another indication that Ce is incorporated in a non-crystalline phase. Na and BH_4 had a ratio of 0.75:1 which signals that signification amounts of Na is also present in an amorphous phase.

4.2.2 In-situ SR-PXD

The in-situ SR-PXD measurements showed that $NaYb(BH_4)_2Cl_2$ and $NaTb(BH_4)_2Cl_2$ decomposed at very different temperatures, T = 130 and 280 °C respectively. This result was surprising because the electronegativites for Yb and Tb are quite similar, suggesting that their decomposition temperature would be closer. During heating peaks from unknown phases appeared in all the samples, indicating that either reactions were activated during heating or that amorphous phases became crystalline. The degree of chloride substitution in the solid-solution, $Na(BH_4)_{1-x}Cl_x$ increased for *Na-Ce-Cl* from RT to 420 °C. Two solid-solutions $Na(BH_4)_{1-x}Cl_x$ were formed in both *Na-Tb-Cl* and *Na-Yb-Cl* with increasing chloride substitution at elevated temperatures.

RE = Yb. Figure 4.17 shows the in-situ SR-PXD measurement of *Na-Yb-Cl*, where the heat map has been divided into temperature regions that indicate when decomposition and formation of phases occurred. At room temperature the sample contained $NaYb(BH_4)_2Cl_2$, Na_3YbCl_6, $YbCl_3$, $NaBH_4$ and one unknown minor phase (Table 4.2). When heated from RT the peak intensity for $NaYb(BH_4)_2Cl_2$ slowly decreased until all the peaks were gone at the end of temperature region **1** (RT-130 °C). Simultaneously peaks from orto$-Yb(BH_4)_2$ and NaCl started to appear, suggesting that they are decomposition products of $NaYb(BH_4)_2Cl_2$. At the start of temperature region **2** the sample was comprised of two solid-solutions of NaCl and $NaBH_4$, where one was NaCl rich and the other $NaBH_4$ rich. Upon heating through temperature region **2** (130-290 °C) Bragg reflections for $YbCl_3$ disappeared, while reflections for the orto$-Yb(BH_4)_2$ phase increased before decomposition of the phase at the end of the region. The Yb_7Cl_{15} phase was formed at the start of temperature region **3** and during further heating there was a clear increase of NaCl in the sample, as the Bragg reflections became more intense and shifted towards lower 2θ values. At the end of temperature region **3** (290-370 °C) the unidentified phase that was present at RT decomposed and peaks from a new unknown phase appeared. Simultaneously the peak intensity for Yb_7Cl_{15} declined while the amount of NaCl kept increasing. In temperature region **4** (370-420 °C) the reflections for Yb_7Cl_{15}, $NaBH_4$ and Na_3YbCl_6 disappeared during heating and YbHCl and $YbCl_2$ were formed. YbHCl and $YbCl_2$ were present at the end of the measurement and are most likely decomposition products of Yb_7Cl_{15} and Na_3YbCl_6, with hydrogen contribution from $NaBH_4$.

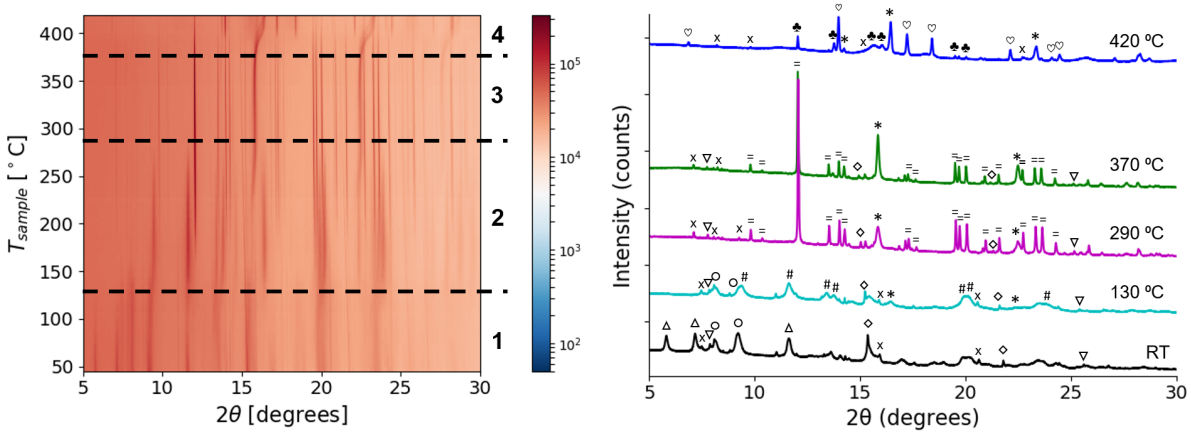

(a) **(b)**

Figure 4.17: **(a)** In-situ SR-PXD of *Na-Yb-Cl* measured from RT to T = 420 °C, $\Delta T/\Delta t = 5$ °C/min ($\lambda = 0.8245$ Å). **(b)** SR-PXD at selected temperatures, where $NaBH_4$ ($\diamond$), $YbCl_3$ ($\circ$), $NaYb(BH_4)_2Cl_2$ ($\triangle$), Na_3YbCl_6 ($\triangledown$), NaCl ($*$), orto$-Yb(BH_4)_2$ (#), Yb_7Cl_{15} ($=$), YbHCl ($\heartsuit$), $YbCl_2$ ($\clubsuit$) and unidentified peaks ($\times$).

RE = Tb. The in-situ SR-PXD measurement of *Na-Tb-Cl* is presented in Figure 4.18. Bragg reflections from $NaTb(BH_4)_2Cl_2$, Na_3TbCl_6, $TbCl_3$ and $NaBH_4$ were observed at RT (Table 4.3). Upon heating the reflections of $NaTb(BH_4)_2Cl_2$ slowly decreased until the phase decomposed at the end of temperature region **1** (RT-280 °C). The decomposition products of $NaTb(BH_4)_2Cl_2$ are most likely amorphous as no new peaks appeared at this temperature. As the sample was heated through temperature region **2** (280-330 °C) the amount of Na_3TbCl_6 decreased and a significant shift in the 2θ position of the Bragg reflections for $Na(BH_4)_{1-x}Cl_x$ was observed. The movement towards larger 2θ indicates a reduction in the unit cell and is assumed to be due to the formation of NaCl. This suggests that Na_3TbCl_6 and $NaBH_4$ reacted to form NaCl and possibly some amorphous products. At the start of temperature region **3** (330-420 °C) the sample consisted of two solid-solutions of NaCl and $NaBH_4$, where one was NaCl rich and the other $NaBH_4$ rich. In temperature region **3** diffraction peaks from $TbCl_3$ decreased and narrow peaks from an unidentified phase appeared at the end of the region.

RE = Ce. At room temperature the sample showed only Bragg reflections of $CeCl_3$ and $Na(BH_4)_{1-x}Cl_x$ (Figure 4.19). During heating through temperature region **1** (RT-310 °C) two new sets of Bragg reflections appeared, while the peak intensities for $CeCl_3$ and $Na(BH_4)_{1-x}Cl_x$ were drastically reduced. One of the sets of Bragg reflections were from NaCl. It seems reasonable to assume that $NaBH_4$ from the solid-solution and $CeCl_3$ reacted, increasing the molar fraction of NaCl in the solid-solution from 0.36 to 0.80, in addition to forming some amorphous phase containing Ce. The other set of peaks corresponded to CeOCl and it therefore, seems as though the sample has been contaminated by air or that the reactants contained some contaminants. Upon further heating in temperature region **2** (310-420 °C) the intensity of the Bragg reflections for CeOCl increased and two Bragg reflections from an unidentified phase were observed at the end of the region. The unknown phase could be the amorphous phase that was formed by the reaction between $NaBH_4$ and $CeCl_3$ and has crystallizing during further heating.

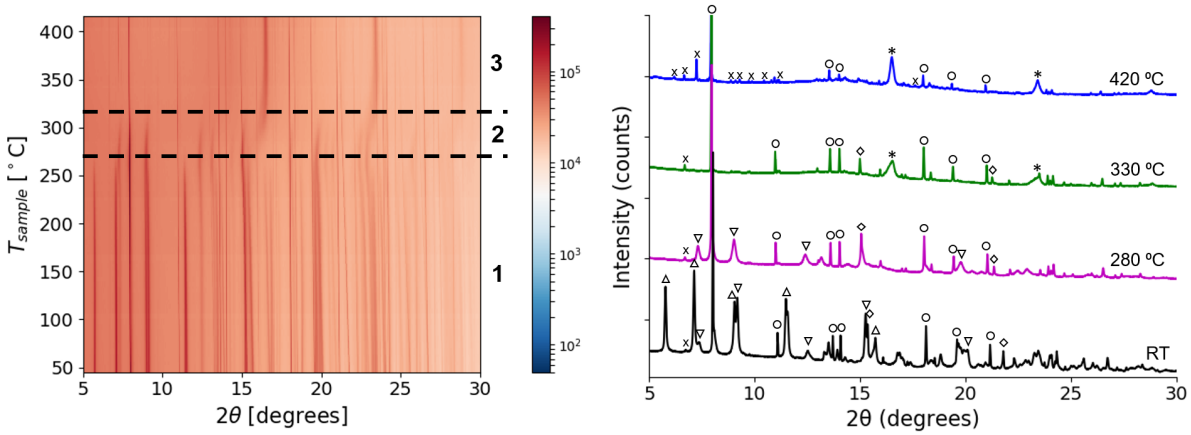

(a) **(b)**

Figure 4.18: **(a)** In-situ SR-PXD of *Na-Tb-Cl* measured from RT to T = 420 °C, $\Delta T/\Delta t = 5$ °C/min ($\lambda = 0.8245$ Å). **(b)** SR-PXD at selected temperatures, where $NaBH_4$ ($\diamond$), $TbCl_3$ ($\circ$), $NaTb(BH_4)_2Cl_2$ ($\triangle$), Na_3TbCl_6 ($\triangledown$), NaCl ($*$) and unidentified peaks ($\times$).

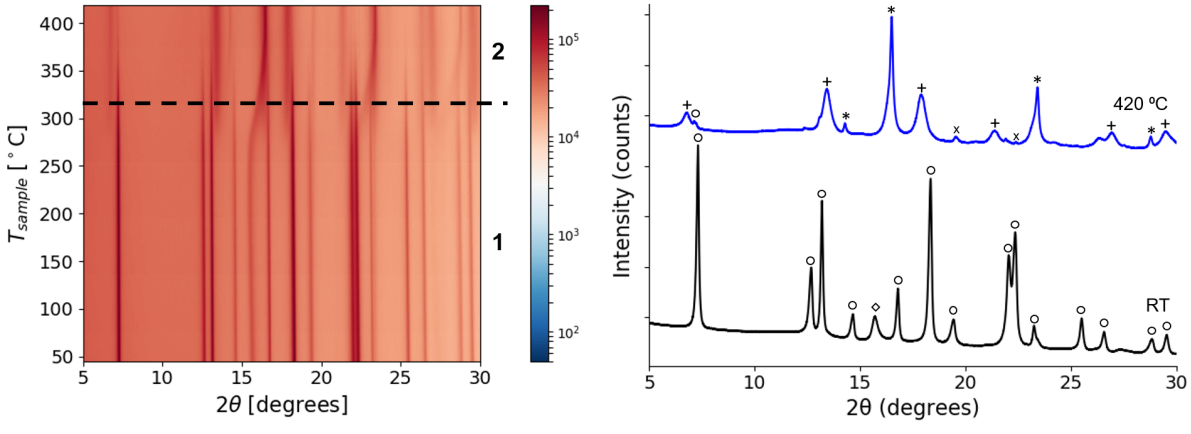

(a) **(b)**

Figure 4.19: **(a)** In-situ SR-PXD of *Na-Ce-Cl* measured from RT to T = 420 °C, $\Delta T/\Delta t = 5$ °C/min ($\lambda = 0.8245$ Å). **(b)** SR-PXD at selected temperatures, where $NaBH_4$ ($\diamond$), $CeCl_3$ ($\circ$), NaCl ($*$), CeOCl ($+$) and unidentified peaks ($\times$).

4.2.3 TGA and DSC measurements

A Kissinger analysis was not conducted for the chloride samples as the TGA-DSC measurements varied greatly from each sample. *Na-Tb-Cl* and *Na-Ce-Cl* showed minor mass losses occurring at T = 300 to 400 °C, indicating the release of small amounts of a volatile material. Like the iodide samples, the decomposition temperatures of the phases were observed to be somewhat lower by TGA and DSC than by in-situ SR-PXD.

RE = Yb. Figure 4.20 presents the TGA-DSC measurements of the as-milled sample from RT to 400 °C with a heating rate of 5 °C/min. By comparing the TGA-DSC data with the in-situ SR-PXD measurement, it seems as though the sample behaved differently during the two types of measurements. The DSC measurement shows an exothermic event with a peak temperature of T = 160°C and a weight loss of 0.75 wt%. It is suggested that $NaYb(BH_4)_2Cl_2$ is a metastable phase and upon heating spontaneously decomposes, which could result in an exothermic event with mass loss. The $NaYb(BH_4)_2Cl_2$ phase had a weight fraction, W_f = 0.290 at RT in the sample. The release of hydrogen during decomposition of $NaYb(BH_4)_2Cl_2$ accounts for a weight loss of 0.79 wt%, which is close to the observed weight loss. From the SR-PXD data orto$-Yb(BH_4)_2$ is assumed to be a decomposition product of $NaYb(BH_4)_2Cl_2$ and decomposes at T = 290 °C. However, the TGA-DSC measurement shows no sign of the orto$-Yb(BH_4)_2$ decomposing at this temperature. There is nor any indication of the formation of Na_3YbCl_6 around T = 300 °C, as seen in the diffraction pattern. The DSC data showed an endothermic peak with a peak temperature T = 382 °C and a weight loss of 0.89 wt%. This event is most likely the decomposition of orto$-Yb(BH_4)_2$ as it is the only remaining phase that contains hydrogen apart from $NaBH_4$, which is stable to 505 °C [45]. The orto$-Yb(BH_4)_2$ phase (W_f = 0.323 at 130 °C) had a hydrogen content of 1.28 wt% in the sample, which is slightly higher than the observed mass loss.

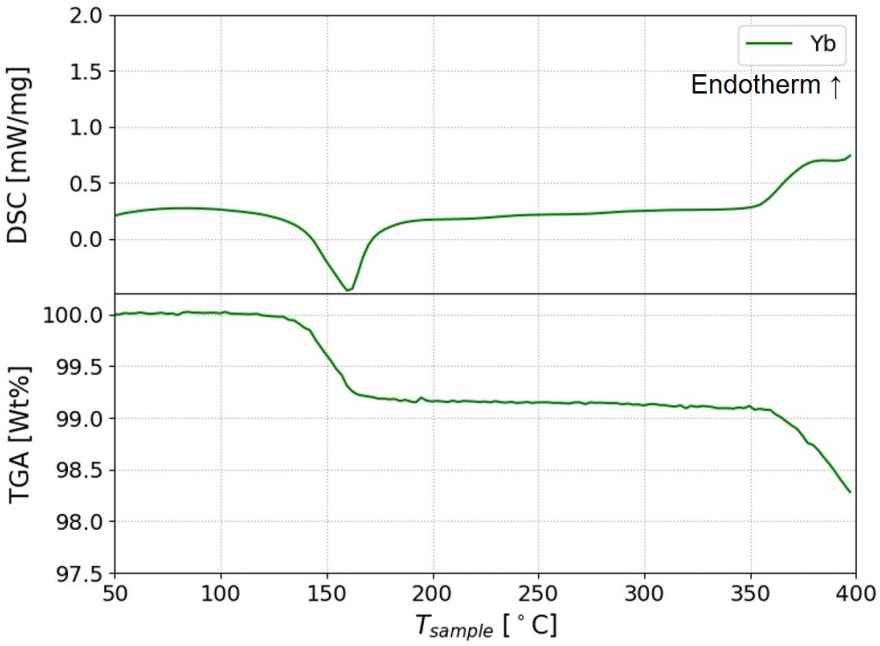

Figure 4.20: Results from simultaneous TGA and DSC measured from RT to T = 400 °C, $\Delta T/\Delta t$ = 5 °C/min for *Na-Yb-Cl*.

RE = Tb. The TGA-DSC measurements from RT to 400°C with a heating rate of 5 °C/min of the as-milled sample is shown in Figure 4.21. In the temperature region of T = 250-300 °C there was a large endothermic peak in the DSC plot, with a peak temperature of T = 279 °C. This event may be due to the decomposition of $NaTb(BH_4)_2Cl_2$ and the reaction between Na_3TbCl_6 and $Na(BH_4)_{1-x}Cl_x$. $NaY(BH_4)_2Cl_2$ was reported to decompose at T = 250-270 °C [45]. Y and Tb have similar Pauling electronegativity's, 1.22 and 1.21 respectively, thus it is expected that the two compounds should have similar decomposition temperatures [58]. The total weight loss of the sample was 2.10 wt%. The hydrogen in $NaTb(BH_4)_2Cl_2$ (W_f = 0.335 at RT) accounts for a weight loss of 0.96 wt% in the sample. It is assumed that some of the weight loss is due to hydrogen release from the reaction between Na_3TbCl_6 and $Na(BH_4)_{1-x}Cl_x$ producing NaCl. Decomposition of an amorphous phase or the release of diborane B_2H_6 or higher boranes can also explain the excess weight loss.

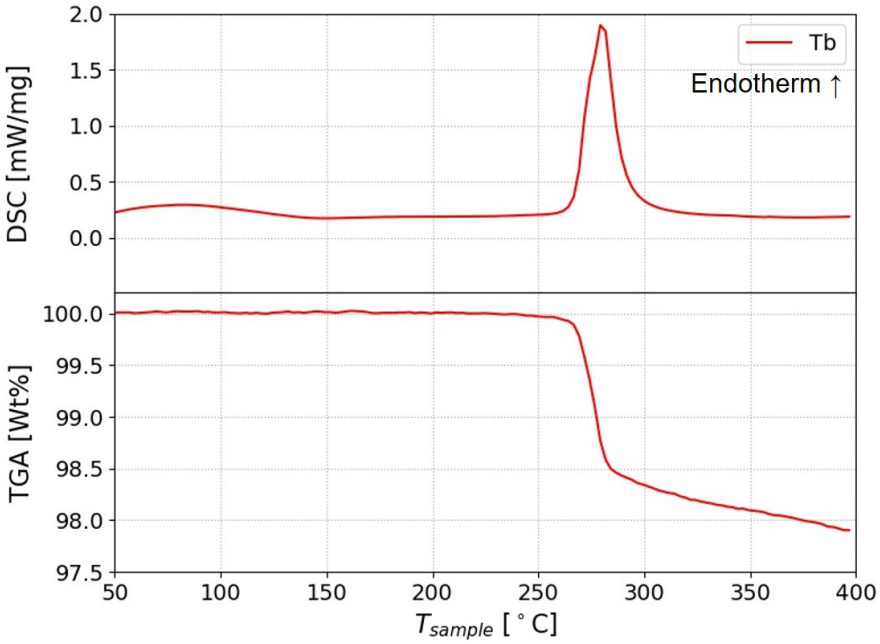

Figure 4.21: Results from simultaneous TGA and DSC measured from RT to T = 400 °C, $\Delta T/\Delta t$ = 5 °C/min for *Na-Tb-Cl*.

RE = Ce. Figure 4.22 shows the TGA-DSC measurements of the as-milled samples from RT to 400 °C with a heating rate of 5 °C/min. The DSC measurement showed two very weak endothermic peaks with peak temperatures at T = 297 and 317 °C. There was an overall weight loss of 1.52 wt% in the sample, where one of the events is most likely due to the increased chloride substitution in $Na(BH_4)_{1-x}Cl_x$. The other peak can be caused by the formation of CeOCl or the decomposition of an amorphous phase.

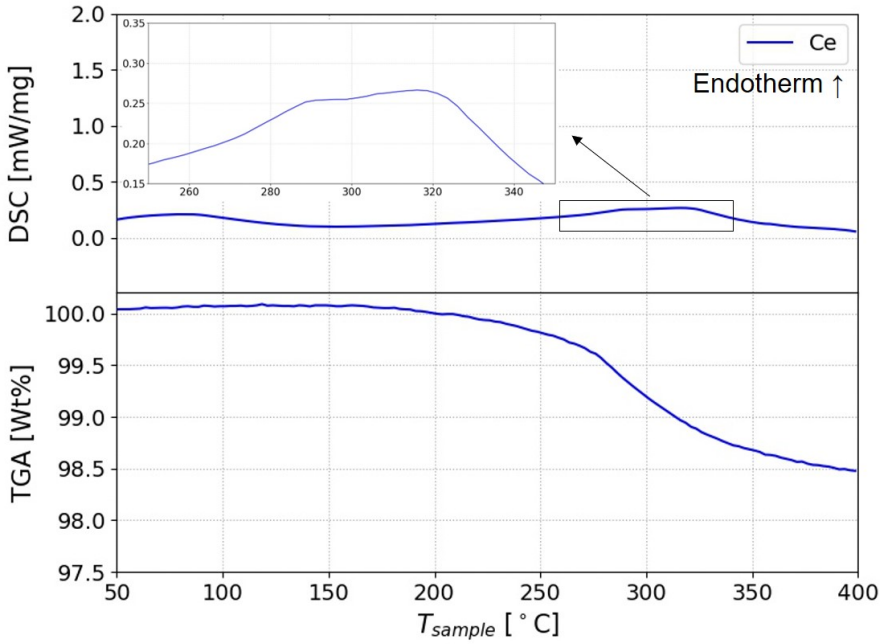

Figure 4.22: Results from simultaneous TGA and DSC measured from RT to $T = 400$ °C, $\Delta T/\Delta t = 5$ °C/min for *Na-Ce-Cl*.

Chapter 5

Further Work

A natural progression of this work is to measure the ionic conductivity of both the $Na_2RE_2(BH_4)_5I_3$ and $NaRE(BH_4)_2Cl_2$ phases, to determine if it is possible to use the material as a solid-state electrolyte for sodium batteries. Both the rare-earth iodides and chlorides have been investigated and have shown very different results. It would, therefore, be compelling to perform similar synthesis with rare-earth bromides, to examine if the samples resemble the iodides, chlorides or form completely new phases.

It would also be of interest to synthesize samples using other rare-earth chlorides and sodium borohydride and investigate if any new phases or other $NaRE(BH_4)_2Cl_2$ phases are formed. This would also allow the opportunity for the assessment of any trends down the rare-earth series. The weight loss in the TGA-DSC measurements for both the iodide and chloride samples were assumed to be mostly hydrogen. Performing mass spectroscopy during TGA-DSC measurements would be informative, as it would give data that could be used to identify the volatile compounds that leave the samples during decomposition.

Further research could also be conducted on achieving a higher yield of the $NaRE(BH_4)_2Cl_2$ phase by altering the milling conditions. Three of the samples were contaminated by oxygen. By investigating where the oxygen came from, contamination of future samples could be avoided.

Chapter 6

Conclusion

This study set out to provide a deeper insight into the rare-earth borohydride halides. A thermal investigation of the iodide samples, *Na-RE-I* (*RE* = Y, Ce, Pr, Nd, Gd, Tb and Er) that were synthesized during Fall 2018, has been conducted. TGA-DSC measurements showed that the $Na_2RE_2(BH_4)_5I_3$ phases decomposed in a single endothermic step in the temperature range of T = 260-280 °C. The results indicated that the onset temperature for the decomposition of $Na_2RE_2(BH_4)_5I_3$ does not change systematically with increased Pauling electronegativity of the rare-earth cation. It was also observed that the activation energies for the decomposition had a positive and almost linear correlation with the cation electronegativity.

High energy ball-milling of $NaBH_4$ and $RECl_3$ (*RE* = Tb and Yb) in a molar ratio of 3:1 resulted in the formation of two new $NaRE(BH_4)_2Cl_2$ phases and Na_3RECl_6. $NaTb(BH_4)_2Cl_2$ and $NaYb(BH_4)_2Cl_2$ were determined to be isostructural to the already reported $NaY(BH_4)_2Cl_2$ phase [45]. As both samples contained significant amounts of the starting materials it was concluded that the synthesis conditions were not optimal. Large amounts of $CeCl_3$ and a solid-solution of $NaBH_4$ and NaCl were observed for the sample synthesized from $NaBH_4$ and $CeCl_3$.

The thermal stability and decomposition routes of the chloride samples were investigated in the same manner as for the iodide samples. The measurements indicated that the decomposition routes for $NaTb(BH_4)_2Cl_2$ and $NaYb(BH_4)_2Cl_2$ were considerably different. $NaTb(BH_4)_2Cl_2$ decomposed in a single step, T_{onset} = 268 °C, where the decomposition product was an amorphous phase. The decomposition route of $NaYb(BH_4)_2Cl_2$ contained multiple reactions and decomposed into orto$-Yb(BH_4)_2$, NaCl and a non-crystalline phase. It was also observed that the *Na-Yb-Cl* sample behaved differently during the in-situ SR-PXD measurement than in the TGA-DSC measurements.

Bibliography

[1] Rana Mohtadi and Shin-ichi Orimo. "The renaissance of hydrides as energy materials". In: *Nature Reviews Materials* 2.3 (2017), p. 16091.

[2] Andreas Züttel. "Materials for hydrogen storage". In: *Materials today* 6.9 (2003), pp. 24–33.

[3] Marit Kolberg, Intisaar Ali, Julie Vissgren, and Marianne Carlsen. "Eksplosjon ved hydrogenstasjon". In: *NRK* (2019). URL: https://www.nrk.no/norge/eksplosjon-ved-hydrogenstasjon-1.14582914.

[4] Mark Paskevicius, Lars H Jepsen, Pascal Schouwink, Radovan Černỳ, Dorthe B Ravnsbæk, Yaroslav Filinchuk, Martin Dornheim, Flemming Besenbacher, and Torben R Jensen. "Metal borohydrides and derivatives, synthesis, structure and properties". In: *Chemical Society Reviews* 46.5 (2017), pp. 1565–1634.

[5] J-Ph Soulié, Guillaume Renaudin, R Černỳ, and Klaus Yvon. "Lithium boro-hydride LiBH4: I. Crystal structure". In: *Journal of alloys and compounds* 346.1-2 (2002), pp. 200–205.

[6] Grigorii L Soloveichik, Yan Gao, Job Rijssenbeek, Matthew Andrus, Sergei Kniajanski, Robert C Bowman Jr, Son-Jong Hwang, and Ji-Cheng Zhao. "Magnesium borohydride as a hydrogen storage material: Properties and dehydrogenation pathway of unsolvated Mg(BH4)2". In: *international journal of hydrogen energy* 34.2 (2009), pp. 916–928.

[7] E Callini, PÁ Szilágyi, M Paskevicius, NP Stadie, J Réhault, CE Buckley, A Borgschulte, and A Züttel. "Stabilization of volatile Ti(BH4)3 by nano-confinement in a metal-organic framework". In: *Chemical science* 7.1 (2016), pp. 666–672.

[8] Line H Rude, Marta Corno, Piero Ugliengo, Marcello Baricco, Young-Su Lee, Young Whan Cho, Flemming Besenbacher, Jacob Overgaard, and Torben R Jensen. "Synthesis and structural investigation of Zr(BH4)4". In: *The Journal of Physical Chemistry C* 116.38 (2012), pp. 20239–20245.

[9] Christoph Frommen, Magnus H Sørby, Michael Heere, Terry D Humphries, Jørn E Olsen, and Bjørn C Hauback. "Rare Earth Borohydrides—Crystal Structures and Thermal Properties". In: *Energies* 10.12 (2017), p. 2115.

[10] Yuko Nakamori, Kazutoshi Miwa, Akihito Ninomiya, Haiwen Li, Nobuko Ohba, Shin-ichi Towata, Andreas Züttel, and Shin-ichi Orimo. "Correlation between thermodynamical stabilities of metal borohydrides and cation electronegativites: First-principles calculations and experiments". In: *Physical Review B* 74.4 (2006), p. 045126.

[11] Yunming Li, Yaxiang Lu, Chenglong Zhao, Yong-Sheng Hu, Maria-Magdalena Titirici, Hong Li, Xuejie Huang, and Liquan Chen. "Recent advances of electrode materials for low-cost sodium-ion batteries towards practical application for grid energy storage". In: *Energy Storage Materials* 7 (2017), pp. 130–151.

[12] Monica Sawicki and Leon L Shaw. "Advances and challenges of sodium ion batteries as post lithium ion batteries". In: *RSC Advances* 5.65 (2015), pp. 53129–53154.

[13] Yumei Wang, Shufeng Song, Chaohe Xu, Ning Hu, Janina Molenda, and Li Lu. "Development of solid-state electrolytes for sodium-ion battery: A short review". In: *Nano Materials Science* (2019).

[14] Morten B Ley, Dorthe B Ravnsbæk, Yaroslav Filinchuk, Young-Su Lee, Raphael Janot, Young Whan Cho, Jørgen Skibsted, and Torben R Jensen. "LiCe(BH4)3Cl, a new lithium-ion conductor and hydrogen storage material with isolated tetranuclear anionic clusters". In: *Chemistry of Materials* 24.9 (2012), pp. 1654–1663.

[15] Christoph Frommen, Magnus Helgerud Sørby, Ponniah Ravindran, Ponniah Vajeeston, H Fjellvag, and BC Hauback. "Synthesis, crystal structure, and thermal properties of the first mixed-metal and anion-substituted rare earth borohydride LiCe(BH4)3Cl". In: *The Journal of Physical Chemistry C* 115.47 (2011), pp. 23591–23602.

[16] M.M.Nygård. "Private communication". 2018.

[17] Emma Berge. "Synthesis and characterization of sodium rare-earth borohydride halides". 2018.

[18] Yaroslav Filinchuk, Dmitry Chernyshov, and Vladimir Dmitriev. "Crystal chemistry of light metal borohydrides". In: *arXiv preprint arXiv:1003.5378* (2010).

[19] Radovan Černỳ and Pascal Schouwink. "The crystal chemistry of inorganic metal borohydrides and their relation to metal oxides". In: *Acta Crystallographica Section B* 71.6 (2015), pp. 619–640.

[20] J-H Her, Peter W Stephens, Yan Gao, Grigorii L Soloveichik, Job Rijssenbeek, Matthew Andrus, and J-C Zhao. "Structure of unsolvated magnesium borohydride Mg(BH4)2". In: *Acta Crystallographica Section B: Structural Science* 63.4 (2007), pp. 561–568.

[21] Line H Rude, Thomas K Nielsen, Dorthe B Ravnsbaek, Ulrike Bösenberg, Morten B Ley, Bo Richter, Lene M Arnbjerg, Martin Dornheim, Yaroslav Filinchuk, Flemming Besenbacher, et al. "Tailoring properties of borohydrides for hydrogen storage: A review". In: *physica status solidi (a)* 208.8 (2011), pp. 1754–1773.

[22] Motoaki Matsuo, Hiroyuki Oguchi, Hideki Maekawa, Hitoshi Takamura, and S Orimo. "Complex Hydrides: A New Category of Solid-State Lithium Fast-Ion Conductors". In: *Mater. Matters* 5 (2010).

[23] Robert D Shannon. "Revised effective ionic radii and systematic studies of interatomic distances in halides and chalcogenides". In: *Acta crystallographica section A: crystal physics, diffraction, theoretical and general crystallography* 32.5 (1976), pp. 751–767.

[24] Borislav Bogdanović, Michael Felderhoff, and Guido Streukens. "Hydrogen storage in complex metal hydrides". In: *Journal of the Serbian Chemical Society* 74.2 (2009), pp. 183–196.

[25] A Züttel, S Rentsch, P Fischer, PMCEP Wenger, PH Sudan, Ph Mauron, and Ch Emmenegger. "Hydrogen storage properties of LiBH4". In: *Journal of Alloys and Compounds* 356 (2003), pp. 515–520.

[26] David Harrison and Timo Thonhauser. "Suppressing diborane production during the hydrogen release of metal borohydrides: The example of alloyed Al(BH4)3". In: *International Journal of Hydrogen Energy* 41.5 (2016), pp. 3571–3578.

[27] Agency for Toxic Substances and Disease Registry. *Medical Management Guidelines for Diborane*. 2014. URL: https://www.atsdr.cdc.gov/MMG/MMG.asp?id=964&tid=202 (visited on 11/29/2018).

[28] Ziheng Lu and Francesco Ciucci. "Metal borohydrides as electrolytes for solid-state Li, Na, Mg, and Ca batteries: a first-principles study". In: *Chemistry of Materials* 29.21 (2017), pp. 9308–9319.

[29] Jørn Eirik Olsen, Christoph Frommen, Torben R Jensen, Marit D Riktor, Magnus H Sørby, and Bjørn C Hauback. "Structure and thermal properties of composites with RE-borohydrides (RE= La, Ce, Pr, Nd, Sm, Eu, Gd, Tb, Er, Yb or Lu) and LiBH4". In: *Rsc Advances* 4.4 (2014), pp. 1570–1582.

[30] Jakob B Grinderslev, Kasper T Møller, Martin Bremholm, and Torben R Jensen. "Trends in Synthesis, Crystal Structure, and Thermal and Magnetic Properties of Rare-Earth Metal Borohydrides". In: *Inorganic chemistry* (2019).

[31] Hans Hagemann, Moise Longhini, Jakub W Kaminski, Tomasz A Wesolowski, Radovan Cerny, Nicolas Penin, Magnus H Sørby, Bjørn C Hauback, Godwin Severa, and Craig M Jensen. "LiSc(BH4)4: a novel salt of Li+ and discrete Sc(BH4)4 complex anions". In: *The Journal of Physical Chemistry A* 112.33 (2008), pp. 7551–7555.

[32] Radovan Cerny, Godwin Severa, Dorthe B Ravnsbæk, Yaroslav Filinchuk, Vincenza D'Anna, Hans Hagemann, Dorthe Haase, Craig M Jensen, and Torben R Jensen. "NaSc(BH4)4: a novel scandium-based borohydride". In: *The Journal of Physical Chemistry C* 114.2 (2009), pp. 1357–1364.

[33] Toyoto Sato, Kazutoshi Miwa, Yuko Nakamori, Kenji Ohoyama, Hai-Wen Li, Tatsuo Noritake, Masakazu Aoki, Shin-ichi Towata, and Shin-ichi Orimo. "Experimental and computational studies on solvent-free rare-earth metal borohydrides R(BH4)3 (R= Y, Dy, and Gd)". In: *Physical Review B* 77.10 (2008), p. 104114.

[34] Christoph Frommen, Nadir Aliouane, Stefano Deledda, Jon Erling Fonneløp, Hilde Grove, Klaus Lieutenant, Isabel Llamas-Jansa, Sabrina Sartori, Magnus H Sørby, and Bjørn C Hauback. "Crystal structure, polymorphism, and thermal properties of yttrium borohydride Y(BH4)3". In: *Journal of Alloys and Compounds* 496.1-2 (2010), pp. 710–716.

[35] Elsa Roedern, Young-Su Lee, Morten B Ley, Kiho Park, Young Whan Cho, Jørgen Skibsted, and Torben R Jensen. "Solid state synthesis, structural characterization and ionic conductivity of bimetallic alkali-metal yttrium borohydrides MY(BH4)4 (M= Li and Na)". In: *Journal of Materials Chemistry A* 4.22 (2016), pp. 8793–8802.

[36] SeyedHosein Payandeh GharibDoust, Michael Heere, Magnus H Sørby, Morten B Ley, Dorthe B Ravnsbæk, Bjørn C Hauback, Radovan Černỳ, and Torben R Jensen. "Synthesis, structure and properties of new bimetallic sodium and potassium lanthanum borohydrides". In: *Dalton Transactions* 45.47 (2016), pp. 19002–19011.

[37] Morten B Ley, Sylvain Boulineau, Raphael Janot, Yaroslav Filinchuk, and Torben R Jensen. "New Li ion conductors and solid state hydrogen storage materials: LiM(BH4)3Cl, M=La, Gd". In: *The Journal of Physical Chemistry C* 116.40 (2012), pp. 21267–21276.

[38] Morten Brix Ley, Mathias Jørgensen, Radovan Cerny, Yaroslav Filinchuk, and Torben R Jensen. "From M(BH4)3 (M= La, Ce) borohydride frameworks to controllable synthesis of porous hydrides and ion conductors". In: *Inorganic chemistry* 55.19 (2016), pp. 9748–9756.

[39] SP GharibDoust, Matteo Brighi, Yolanda Sadikin, Dorthe Bomholdt Ravnsbæk, Radovan Černỳ, TR Jensen, and J Skibsted. "Synthesis, Structure and Li Ion Conductivity of LiLa(BH4)3X, X= Cl, Br, I". In: *J. Phys. Chem. C* 121 (2017), pp. 19010–19021.

[40] SeyedHosein Payandeh GharibDoust, Michael Heere, Carlo Nervi, Magnus H Sørby, Bjørn C Hauback, and Torben R Jensen. "Synthesis, structure, and polymorphic transitions of praseodymium (III) and neodymium (III) borohydride, Pr(BH4)3 and Nd(BH4)3". In: *Dalton Transactions* 47.25 (2018), pp. 8307–8319.

[41] Wojciech Wegner, Tomasz Jaroń, and Wojciech Grochala. "Polymorphism and hydrogen discharge from holmium borohydride, Ho(BH4)3, and KHo(BH4)4". In: *international journal of hydrogen energy* 39.35 (2014), pp. 20024–20030.

[42] Jørn Eirik Olsen, Christoph Frommen, Magnus H Sørby, and Bjørn C Hauback. "Crystal structures and properties of solvent-free LiYb(BH4)4-xClx, Yb(BH 4)3 and Yb(BH4)2-xClx". In: *Rsc Advances* 3.27 (2013), pp. 10764–10774.

[43] Wojciech Wegner, Tomasz Jaroń, and Wojciech Grochala. "MYb(BH4)4 (M= K, Na) from laboratory X-ray powder data". In: *Acta Crystallographica Section C: Crystal Structure Communications* 69.11 (2013), pp. 1289–1291.

[44] Anthony R West. *Solid state chemistry and its applications*. John Wiley & Sons, 2014.

[45] Dorthe B Ravnsbæk, Morten B Ley, Young-Su Lee, Hans Hagemann, Vincenza D'Anna, Young Whan Cho, Yaroslav Filinchuk, and Torben R Jensen. "A mixed-cation mixed-anion borohydride NaY(BH4)2Cl2". In: *international journal of hydrogen energy* 37.10 (2012), pp. 8428–8438.

[46] Michael Heere, Seyed Hosein Payandeh GharibDoust, Christoph Frommen, Terry D Humphries, Morten B Ley, Magnus H Sørby, Torben R Jensen, and Bjørn C Hauback. "The influence of LiH on the rehydrogenation behavior of halide free rare earth (RE) borohydrides (RE= Pr, Er)". In: *Physical Chemistry Chemical Physics* 18.35 (2016), pp. 24387–24395.

[47] M Weller, T Overton, J Rourke, and F Amstrong. *Inorganic chemistry 6th edition*. 2014.

[48] Richard JD Tilley. *Understanding solids: the science of materials*. Wiley, 2013.

[49] Industrial Liaison Team at Diamond. *Powder Diffraction for Industry*. URL: https://www.diamond.ac.uk/industry/Industry-News/Latest-News/Synchrotron-Industry-News-Powder-Diffraction.html (visited on 11/26/2018).

[50] A Albinati and BTM Willis. "The Rietveld method in neutron and X-ray powder diffraction". In: *Journal of Applied Crystallography* 15.4 (1982), pp. 361–374.

[51] Robert E Dinnebier, Andreas Leineweber, and John SO Evans. *Rietveld Refinement: Practical Powder Diffraction Pattern Analysis Using TOPAS*. Walter de Gruyter GmbH & Co KG, 2018.

[52] J Farjas and P Roura. "Exact analytical solution for the Kissinger equation: determination of the peak temperature and general properties of thermally activated transformations". In: *Thermochimica acta* 598 (2014), pp. 51–58.

[53] Bruker. *EVA Software - The next era in phase analysis*. URL: https://www.bruker.com/products/x-ray-diffraction-and-elemental-analysis/x-ray-diffraction/xrd-software/eva/overview.html (visited on 2019).

[54] ICDD. *Phase Identification Quantitation*. URL: http://www.icdd.com/index.php/pdf-4/ (visited on 2019).

[55] Vincent Favre-Nicolin and Radovan Černỳ. "FOX,free objects for crystallography': a modular approach to ab initio structure determination from powder diffraction". In: *Journal of Applied Crystallography* 35.6 (2002), pp. 734–743.

[56] Brian H Toby and Robert B Von Dreele. "GSAS-II: the genesis of a modern open-source all purpose crystallography software package". In: *Journal of Applied Crystallography* 46.2 (2013), pp. 544–549.

[57] FIZ Karlsruhe. *ICSD Phase Identification Quantitation*. URL: https://icsd.fiz-karlsruhe.de/index.xhtml;jsessionid=D1FF291C5BCC60F439B693013D144257 (visited on 2019).

[58] James E Huheey, Ellen A Keiter, Richard L Keiter, and Okhil K Medhi. *Inorganic chemistry: principles of structure and reactivity*. Pearson Education India, 2006.

[59] Eugen Posnjak and Ralph WG Wyckoff. "The crystal structures of the alkali halides. II". In: *Journal of the Washington Academy of Sciences* 12.10 (1922), pp. 248–251.

[60] WH Zachariasen. "Crystal chemical studies of the 5f-series of elements. I. New structure types". In: *Acta Crystallographica* 1.5 (1948), pp. 265–268.

[61] JD Forrester, Allan Zalkin, David H Templeton, and JC Wallmann. "Crystal structure of terbium trichloride". In: *Inorganic Chemistry* 3.2 (1964), pp. 185–188.

[62] SI Troyanov. "Crystal Structure of Ti(AlCl4)2 and Refinement of the Crystal Structure of AlCl3." In: *ChemInform* 23.43 (1992), no–no.

[63] Liesbet Jongen and Gerd Meyer. "Yttrium triiodide, YI3". In: *Acta Crystallographica Section E: Structure Reports Online* 61.8 (2005), pp. i151–i152.

[64] Gerd Meyer. "Na3GdCl6: Einkristalle der Tieftemperaturform bei der metallothermischen Reduktion von GdCl3 mit Na". In: *Zeitschrift für anorganische und allgemeine Chemie* 517.10 (1984), pp. 191–197.

[65] OG Potapova, IG Vasil'eva, and SV Borisov. "Crystal structure of praseodymium oxide iodide". In: *Journal of Structural Chemistry* 18.3 (1977), pp. 459–462.

[66] Bo Richter, Jakob B Grinderslev, Kasper T Møller, Mark Paskevicius, and Torben R Jensen. "From Metal Hydrides to Metal Borohydrides". In: *Inorganic chemistry* 57.17 (2018), pp. 10768–10780.

[67] Christian Rinck. *Röntgenographische Strukturuntersuchungen an Seltenerdmetall (II, III)-chloriden des Formeltyps LnmCl2m+1 (Ln*. Roland Flaxmeier. Offsetdruck, 1982.

[68] D Rudolph and T Schleid. "Single crystals of matlockite-type YbHCl". In: *Zeitschrift fuer Kristallographie. Supplement* 35 (2015), pp. 84–85.

[69] Horst P Beck and H Bärnighausen. "Zur Kristallchemie der Ytterbium (II)-Halogenide YbCl2 und YbBr2". In: *Zeitschrift für anorganische und allgemeine Chemie* 386.2 (1971), pp. 221–228.

Appendix A

Sample Preparation

A.1 Chloride samples, *Na-RE-Cl*

Table A.1: Mass and molar composition of *Na-RE-I* samples.

Sample	$\frac{n_{NaBH_4}}{n_{RECl_3}}$ [∅]	m_{tot} [g]	m_{RECl_3} [g]	m_{NaBH_4} [g]	n_{RECl_3} [mol]	n_{NaBH_4} [mol]
Na-Ce-Cl	$\frac{5}{3}$	1.001	0.797	0.204	0.00323	0.00539
Na-Tb-Cl	3	1.001	0.701	0.300	0.00264	0.00793
Na-Yb-Cl	3	1.000	0.711	0.289	0.00254	0.00763

A.2 Iodide samples, *Na-RE-I*

Table A.2: The abbreviated names and the initial composition of the samples, together with the crystal structures of the various rare earth iodides.

Sample	Initial composition	Structure of REI$_3$
Na-Y-I	3NaBH$_4$ + YI$_3$	Trigonal ($R\bar{3}h$)
Na-Ce-I	3NaBH$_4$ + CeI$_3$	Orthorhombic ($Cmcm$)
Na-Pr-I	3NaBH$_4$ + PrI$_3$	Orthorhombic ($Cmcm$)
Na-Nd-I	3NaBH$_4$ + NdI$_3$	Orthorhombic ($Cmcm$)
Na-Gd-I	3NaBH$_4$ + GdI$_3$	Trigonal ($R\bar{3}h$)
Na-Tb-I	3NaBH$_4$ + TbI$_3$	Trigonal ($R\bar{3}h$)
Na-Er-I	3NaBH$_4$ + ErI$_3$	Trigonal ($R\bar{3}h$)

Table A.3: Mass and molar composition of *Na-RE-Cl* sample.

Sample	$\frac{n_{NaBH_4}}{n_{REI_3}}$ [∅]	m_{tot} [g]	m_{REI_3} [g]	m_{NaBH_4} [g]	n_{REI_3} [mol]	n_{NaBH_4} [mol]
Na-Y-I	3	1.000	0.805	0.195	0.00171	0.00514
Na-Ce-I	3	1.000	0.821	0.179	0.00158	0.00473
Na-Pr-I	3	1.000	0.821	0,179	0.00157	0.00472
Na-Nd-I	3	1.000	0.822	0.178	0.00157	0.00470
Na-Gd-I	3	1.000	0.826	0.174	0.00154	0.00461
Na-Tb-I	3	1.000	0.826	0.174	0.00153	0.00459
Na-Er-I	3	1.001	0.829	0.172	0.00151	0.00454

Appendix B

Laboratory PXD

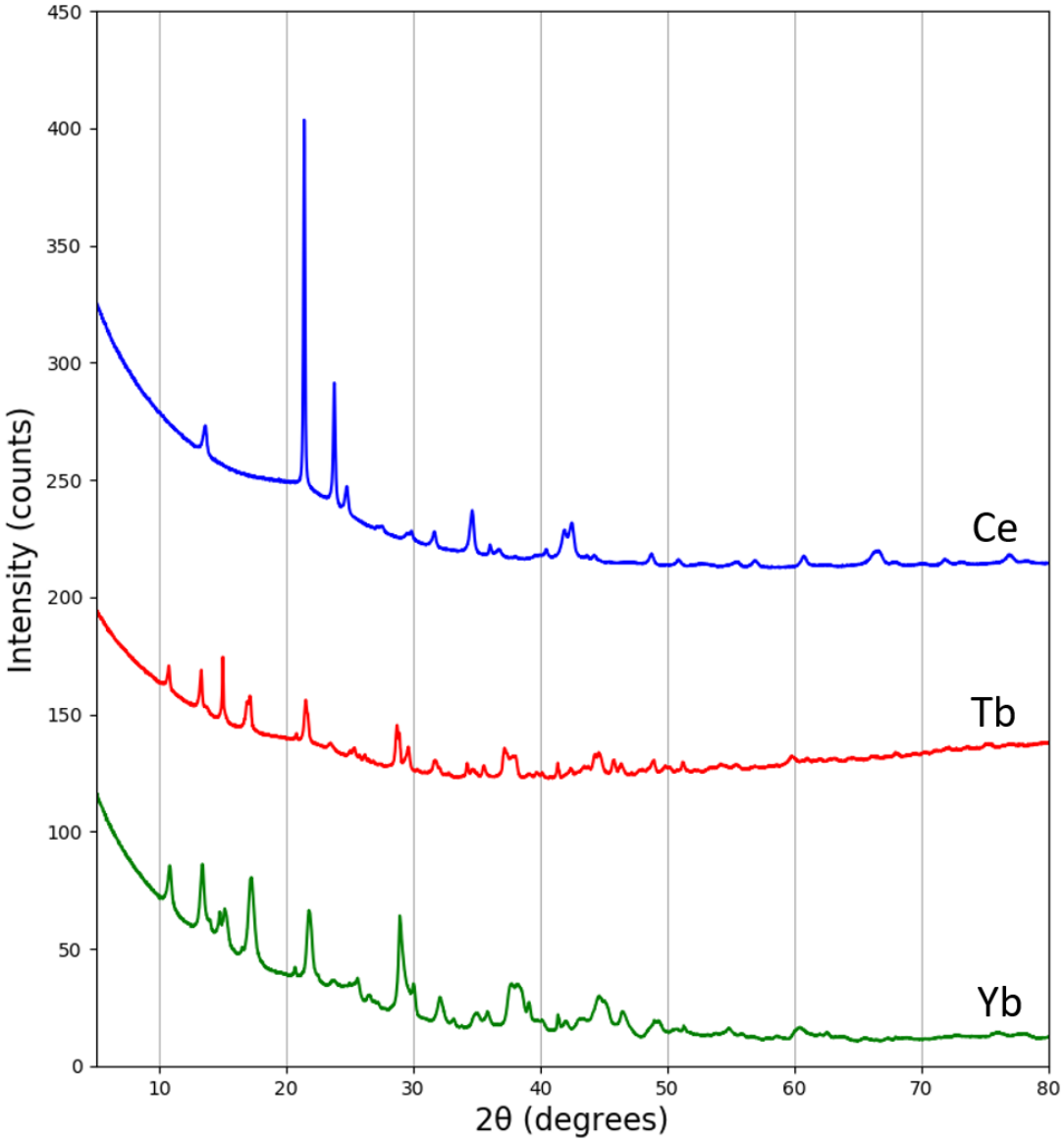

Figure B.1: Laboratory PXD measurements of the *Na-RE-Cl* samples.

Appendix C

Crystal Information Files

Table C.1: Crystal Information Files used for phases in the Rietveld refinements.

Phase	Crystal System	Space Group	Ref.
$NaBH_4$	Cubic	$Fm\bar{3}m$	[35]
NaX (X = I and Cl)	Cubic	$Fm\bar{3}m$	[59]
$CeCl_3$	Hexagonal	$P63/m$	[60]
$TbCl_3$	Orthorhombic	$Cmcm$	[61]
$YbCl_3$	Monoclinic	$C2/m$	[62]
REI_3 (*RE* = Ce, Pr and Nd)	Orthorhombic	$Cmcm$	[60]
REI_3 (*RE* = Y, Gd and Tb)	Trigonal	$R\bar{3}h$	[63]
α-$RE(BH_4)_3$ (*RE* = Y, Gd, Tb and Er)	Cubic	$Pa\bar{3}$	[35]
$NaRE(BH_4)_2Cl_2$ (*RE* = Tb and Yb)	Monoclinic	$P2/c$	[45]
Na_3RECl_6 (*RE* = Tb and Yb)	Trigonal	$R\bar{3}h$	[64]
*RE*OI (*RE* = Gd and Er)	Tetragonal	$P4/nmm$	[65]
CeOCl	Tetragonal	$P4/nmm$	[65]
$Yb(BH_4)_2$	Orthorhombic	$Pbca$	[66]
Yb_7Cl_{15}	Orthorhombic	$Pnma$	[67]
YbHCl	Tetragonal	$P4/nmm$	[68]
$YbCl_2$	Orthorhombic	$Pbca$	[69]